Investigation of some 4*d* and 5*d* transition metal based Double Perovskites

A Thesis

submitted to

Indian Institute of Science Education and Research Pune

in partial fulfilment of the requirements for the

BS-MS Dual Degree Programme

by

Haritha S V

Indian Institute of Science Education and Research Pune

Dr. Homi Bhabha Road,

Pashan, Pune 411008, INDIA.

April, 2020

Supervisor: Dr. Sunil Nair

Certificate

This is to certify that this dissertation entitled ***Investigation of some 4d and 5d transition metal based Double Perovskites*** towards the partial fulfilment of the BS-MS dual degree programme at the Indian Institute of Science Education and Research, Pune represents study/work carried out by **Haritha S V** at Indian Institute of Science Education and Research under the supervision of **Dr. Sunil Nair**, associate Professor, Department of Physics, during the academic year 2019-2020.

Student

Haritha S V

Supervisor

Dr. Sunil Nair

Committee: Physics

Dr. Sunil Nair

Dr. Surjeet Singh

Declaration

I hereby declare that the matter embodied in the report entitled ***Investigation of some 4d and 5d transition metal based Double Perovskites*** are the results of the work carried out by me at the Department of Physics, Indian Institute of Science Education and Research, Pune, under the supervision of Dr. Sunil Nair and the same has not been submitted elsewhere for any other degree.

Student

Haritha S V

Supervisor

Dr. Sunil Nair

Acknowledgments

I would like to thank Dr. Sunil Nair for his constant support and guidance during this work. His enthusiasm and passion for science have motivated me to pursue research. I would like to thank him for giving me an opportunity to try instrumentation and also for his support during difficult times. I express my sincere gratitude to Shruti Chakravarty for introducing me to the lab and the research work. I am thankful for her guidance throughout my time in the lab and all the good moments I had with her. I thank Avirup De, Dr. Jitender Thakur, for their guidance during instrumentation and Charu Garg for valuable suggestions in solid-state synthesis. I also thank Anna Merin Francis, Bicky, Dr. Mousmi Sen, and Dr. Shruti. I would like to thank the technical staff at $\hbar$; Nilesh Dumbre, Anil Prathamashetti, and Sudhir for their help during the project. I would like to express my gratitude to Dr. Surjeet Singh, my TAC, for his guidance in the project and academics. A special thanks to TIFR, where the heat capacity measurements were carried out. I thank my friends Felix, Nazia, Adityan, Anjana, Feba, Shivani Lomte, and Athunya for making this time memorable and for their love and support. Finally, I would like to thank my parents and sister for their constant support and for believing in me.

Contents

List of Tables

Part1: Synthesis and characterization of 3*d*-5*d* transition metal based Double Perovskites

List of Figures

Part1: Synthesis and characterization of 3*d*-5*d* transition metal based Double Perovskites

Abstract

Iridium based Double Perovskites have been of keen interest in solid-state Physics due to the intricate interplay of fundamental interactions like spin-orbit coupling, electron bandwidth, on-site Coulombic force, and crystal field energy. The dynamics between these forces and electron degrees of freedom (charge, spin, and orbital) result in novel electronic and magnetic ground states. During this project, Double Perovskites; Ba_2FeIrO_6, $Y_2(Ni/Co)IrO_6$ are synthesized via solid-state route. Ba_2FeIrO_6 with Ir in 5^+ oxidation state crystallizes in a hexagonal structure. Due to the similarity in ionic radii of two transition metal cations, it possesses high antisite disorder. This also reflects in its molar heat capacity measurement, which shows evidence of a glassy phase. $Y_2(Ni/Co)IrO_6$, on the other hand, has iridium in the 4^+ oxidation state and crystallizes in monoclinic structure. The octahedral tilt occurring to compensate the small *A* cation size results in a high magnetic order temperature of 186K in Y_2NiIrO_6. The data obtained corroborate with the strong magneto-structural coupling observed in the Ln_2NiIrO_6 series. Molar heat capacity studies indicate the presence of glassy phase at low temperature.

The development of an automated susceptometer for measuring linear and non-linear dielectric response has also been a part of the project. The design principles, as well as the calibration of the instrument using the first harmonic response of a standard dielectric sample KH_2PO_4 is described.

Part 1: Synthesis and characterization of 3*d*-5*d* transition metal based Double Perovskites

Chapter 1 Introduction

1.1 Perovskites

Perovskites are an interesting group of oxides due to their compositional and structural flexibility. They have ABO_3 formula where the large A cations are typically from alkaline earth elements, and smaller B cations are transition metals. In an ideal cubic Perovskite shown in Figure 1.1(a), A cations are at a twelve-coordinated site while B cations sit at the center of a corner-shared oxygen octahedra. A large number of cations can be substituted at these A, B sites and what is more interesting is that one can do partial doping at individual sites. This leads to a plethora of interactions within the system and hence exciting physical properties emerge. A 1:1 doping at the B site gives $A_2B^{'}B^{''}O_6$, named as Double Perovskites and has unit cell dimensions double those of ABO_3, shown in Figure 1.1(b).

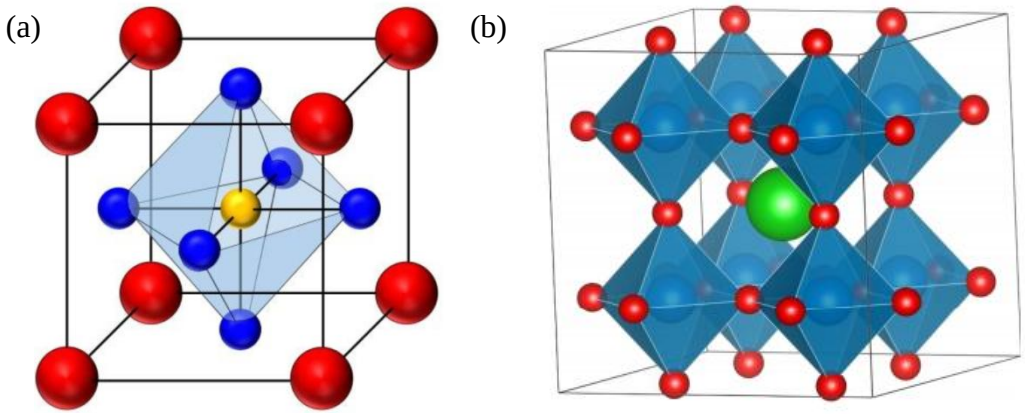

Figure 1.1 (a) Unit cell of a Perovskite compound. Red, yellow, and blue atoms are A, B, and oxygen respectively [1] (b) Unit cell of a Double Perovskite compound. A cation sits in the void created by oxygen octahedra [2].

Since larger size or lower oxidation state of A cation provides more possibilities for the B cations, Double Perovskites with divalent A cations are the most reported while trivalent are the second most reported [3]. For a divalent A cation, possible B cation combinations are the following: $(1^+, 7^+)$, $(2^+, 6^+)$, $(3^+, 5^+)$, $(4^+,4^+)$. Likewise for a trivalent A cation, possible B cation combinations are listed: $(1^+, 5^+)$, $(2^+, 4^+)$, $(3^+, 3^+)$. This covers a series of transition metals, lanthanoids, actinoids and some of the main group elements as well. Since B cations predominantly govern the magnetic and electrical properties of the system, novel combinations could lead to an exotic ground state. But not all of these combinations will result in an ideal cubic Perovskite structure; nonetheless, BO_6 octahedra can contract, expand,

tilt or distort accordingly [4-5]. Cation size mismatch between *A* and *B* are indicated by Goldschmidt tolerance factor [6],

$$t = \frac{r_A + r_B}{\sqrt{2}(r_B + r_O)}$$

Where r_A, r_B, r_O are ionic radii of *A*, *B* cations and oxygen respectively. In the case of $A_2B'B''O_6$, an average of *B* cation radii is considered as r_B. For an ideal cubic Perovskite, tolerance factor *t* is one. A value less than one indicates *A* cation size is less than ideal and this is compensated by a tilt or a bond length change in the octahedra [7]. But larger A cation results in non-perovskite structures [8]. Tilting and consequent changes in the bond length and angles also affect the physical properties of the system. From a review of reported Double Perovskites till date, Vasala and Karppinen estimated the possible *t* range, t = 0.85 - 1.05, where a Perovskite phase can be stabilized [3].

1.1.1 Transition metal-based Double Perovskites

As mentioned earlier, *B* cations predominantly govern electrical and magnetic properties of the system. Interesting properties emerge when a combination of transition metals are used at the *B* site, especially *3d-4d/5d* elements. An electron in a solid has three degrees of freedom: charge, spin, and orbital. Also, there are fundamental interactions between electrons such as on-site Coulombic force, Spin-Orbit Coupling (SOC), crystal field energy. Dynamics between electron degrees of freedom and fundamental interactions lead to exciting ground states. Having two different *B* cations itself increases the complexity of the system. To enhance the delocalization of electrons; orbital energy overlap, spatial overlap, and symmetry of the two orbitals are necessary. For example, if *B*' is a transition metal and *B*" is from the main block, then orbital overlap will not occur due to symmetry. Even if both *B*' and *B*" are from transition metal series, if their band energy is very different, mixing will not happen. Along with these considerations, *3d* and *4d/5d* series have their own unique identities. *3d* elements have comparable crystal field splitting energy and on-site Coulombic interaction, hence they usually have high spin states. But 4*d*/5*d* transition metals have relatively weaker on-site Coulombic interaction and higher crystal field splitting energy due to the extended orbitals. Thus 4*d*/5*d* elements are found in low spin states in t_{2g} band. Having all these complexities, Double Perovskites with 3*d*-4*d*/5*d* combination exhibit electronic ground states ranging from insulators [9] to metallic [10], half-metallic [11], superconductors [12], ferroelectric [13] and so on. In terms of magnetic properties also, the 3*d*-4*d*/5*d* combination

exhibits impressive diversity. It ranges from antiferromagnets [14] to ferro- [15] and ferrimagnets. In the presence of cation disorder, geometrical or magnetic lattice frustration, spin glass [16] or spin liquid state [17] also emerges. In $A_2B'B''O_6$ with single paramagnetic *B* cation, superexchange interactions can be over long distances. But in Double Perovskites with two different B cations, interactions are complicated. There can be B'-O-B'' short-distance interactions, B'-O-(B'')-O-B', or B''-O-(B')-O-B''. Which of these dominates depends on the orbital symmetry, extend of energy orbital overlap [18], and spatial orbital overlap [19].

1.1.2 Why Iridium (Ir) based Double Perovskites?

Iridates are interesting due to the unique interplay of fundamental interactions: Spin-Orbit Coupling (SOC), on-site Coulombic repulsion, and crystal field energy. In addition to these competing interactions, Iridates also have an advantage of spatially extended *5d* orbitals which promotes delocalization of electrons via metal-oxygen hybrid bonds. Hence, Iridates are expected to be more metallic but less magnetic. But experimental observations show deviations from this trend [20-22]. To understand this, we need to remember that Iridium, a *5d* transition metal with atomic number 77, possesses a high spin orbit coupling (SOC). SOC experienced by the outermost electrons in an atom is proportional to Z^2 [23] and in case of Ir, this is equal to 0.4eV whereas for a 3*d* transition metal this value is far less (~20 meV). Figure 1.2 shows how SOC lifts the degeneracy of a 5*d* orbital. Strong SOC further splits the t_{2g} band into $J_{3/2}$ and $J_{1/2}$ with the former having lower energy. In the case of Ir^{4+}, four electrons are filled in $J_{3/2}$ and the last electron in $J_{1/2}$. The dynamics between on-site Coulombic repulsion and SOC create a narrow bandgap in $J_{1/2}$ favoring a Mott insulator state. This is observed in Ruddleson-Popper phases $Sr_{n+1}Ir_nO_{3n+1}$ and the gap in $J_{1/2}$ reduces as the dimensionality n increases. Consequently, from Sr_2IrO_4 (n=1) to SrIrO3 (n=∞), ground state changes from insulating to metallic state [24]. Considering Ir^{5+} states, splitting of t_{2g} and distribution of 4 electrons, results in J_{eff} = 0.This means a non-magnetic ground state is predicted for an Ir^{5+} state where SOC is much stronger than any other interactions. But when SOC, on-site coulombic interaction and crystal field energy are comparable, they compete with each other. These result in novel ground states and lattice distortions have a larger role in making this possible [25-27]. Sr_2YIrO_6, a well-studied system in this regime undergoes an anti-ferromagnetic transition at 1.3K [28]. Here, Yttrium replaces every alternate Iridium cation and no inter-site disorder is expected between these two cations due to differences in

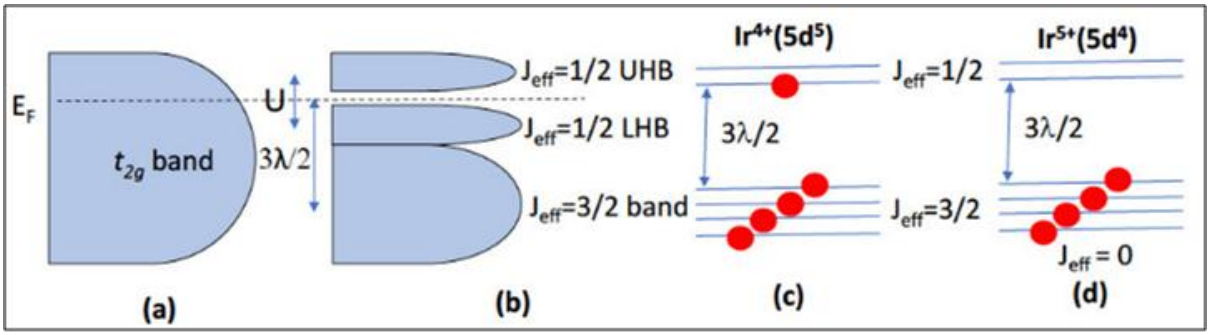

Figure 1.2 (a) t_{2g} band of 5d electrons. (b) Splitting of t_{2g} orbital into $J_{3/2}$ and $J_{1/2}$ due to SOC (λ). (c) Electron arrangement in $5d^5$ state. The fifth electron resides in the lower $J_{1/2}$ band where the Fermi energy level resides. (d) Electron arrangement of $5d^4$ state [23]

both oxidation state and ionic radii. This results in a Face Centered Cubic (FCC) lattice with geometrically frustrated edge-sharing tetrahedra of Ir ions. BO_6 octahedra are highly tilted creating a non-cubic crystal field around the Ir^{5+} ions. Another magnetic ground state possible in Ir^{5+} compounds results from the hopping from $J_{3/2}$ to $J_{1/2}$ [26-27]. As hopping increases, the bandwidth of $J_{3/2}$ increases and may result in an overlap of two orbitals. Hence, $J_{1/2}$ can be partially filled with electrons while $J_{3/2}$ is filled by holes, giving an effective non-zero J value. This has been used to explain the presence of magnetic ordering in distorted Sr_2YIrO_6, cubic Ba_2YIrO_6 and the $(Ba_{1-x}Sr_x)_2YIrO_6$ series [29]. But what is unique to this magnetic state is that it is very weak and unstable compared to the J_{eff}= 0 state or S=1 state usually seen in heavy d^4 ions. Even though Ir^{5+} is not expected to have any magnetic moment, it is intriguing that how sensitive its ground state is to chemical environment and lattice.

1.2 Spin glass

This class of materials undergoes a continuous phase transition into a frozen state of spins as a result of cooperative freezing of all spins at a particular temperature T_f. Transition into a glass breaks the time-reversal symmetry and has a unique order parameter as well. There are several experimental features that glassy materials possess [30]. In an AC susceptibility measurement as a function of temperature, glasses show a maximum at T_f. This is because, near the freezing temperature T_f, the relaxation time increases, resulting in a maximum in the measured susceptibility signal. This maximum is dependent on the AC field frequency. As frequency reduces, the peak shifts to lower temperatures. Figure 1.3 shows the AC susceptibility response of a spin glass CuMn.

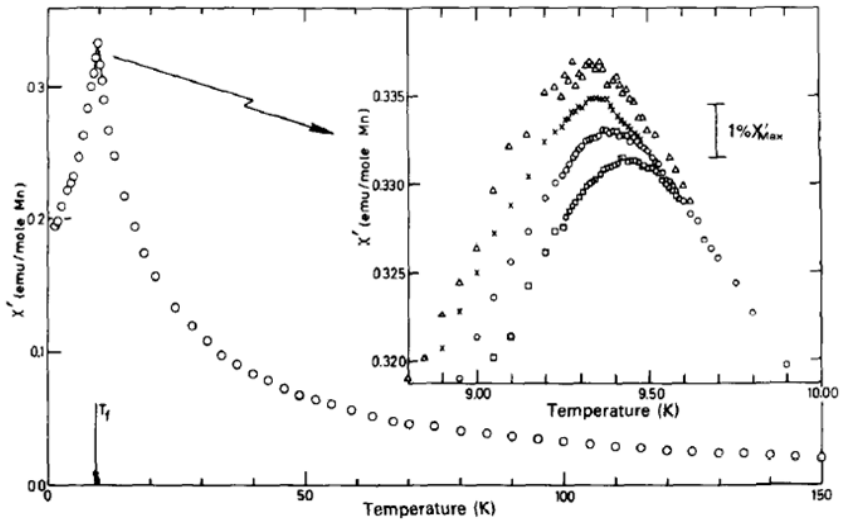

Figure 1.3 AC susceptibility measurement of CuMn as a function of temperature. Inset shows frequency dependence of the peak maximum [32]

The second feature of spin glasses is seen in the DC magnetization during ZFC (Zero Field Cooled) and FC (Field Cooled) measurements (Figure 1.4). ZFC and FC curves diverge below T_f and an application of the magnetic field to the ZFC state results in a time-dependent increase in *M(H)*. The third criterion is the magnetic specific heat measurement C_m which follows temperature linearly at low temperature and presents a broad maximum at 20-40% above T_f. Then C_m falls of as 1/T (Figure 1.5). These features clearly distinguish glasses from long-range ordered magnetic materials as they exhibit an anomaly at magnetic transition temperature followed by an abrupt decrease in C_m magnitude. The aging process is also used to study meta-stable spin glasses.

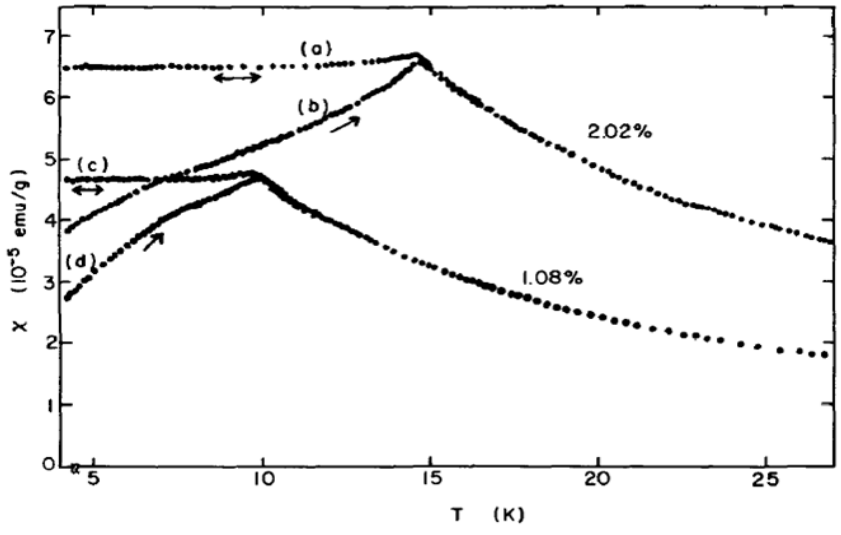

Figure 1.4 ZFC, FC susceptibility for CuMn in 6 Oe field [33]

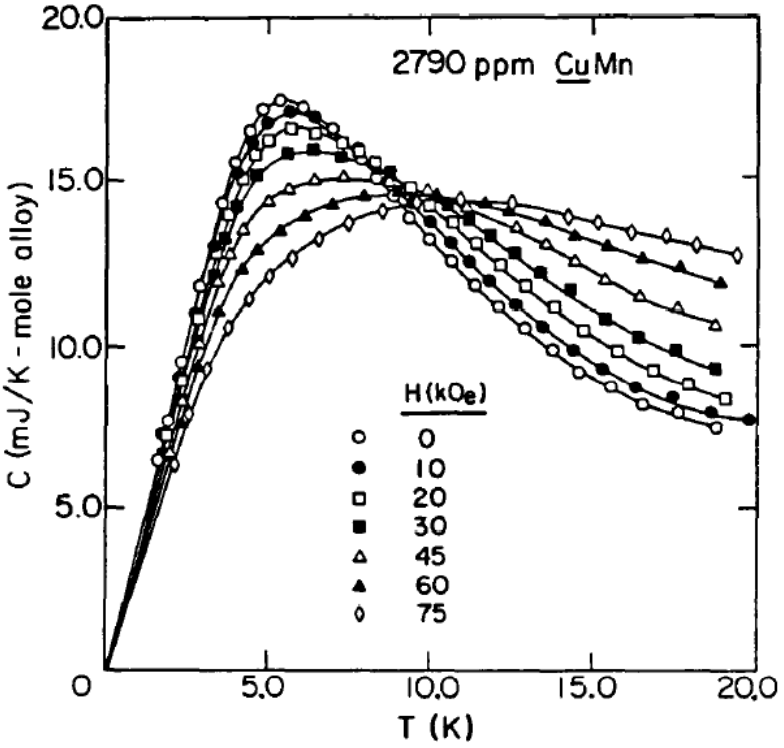

Figure 1.5 Magnetic specific heat as a function of temperature [34].

Randomness in the magnetic lattice either through the distribution of magnetic ion or through random interactions, geometrical frustration (e.g. triangular lattice), and competing interactions are the three ingredients of a spin glass [31]. But all three ingredients are not necessary for the SG phase; rather any one of them, with a small amount of another is enough to induce glassiness in the system.

1.3 Ba_2FeIrO_6: a potential spin glass

Ba_2FeIrO_6 is a Double Perovskite with Ir in +5 oxidation state ($5d^4$) and Fe in +3 oxidation state ($3d^5$). If we consider the individual perovskite phases; $BaFeO_{3-\delta}$ with 12H structure has a transition to ferromagnetic (FM) state at around 250K and to an anti-ferromagnetic (AFM) state at around 160K [35], whereas the $BaIrO_{3-\delta}$ with 9R hexagonal structure exhibits a ferromagnetic transition around 180K [36]. So, it would be very interesting to study the magnetic ground state of a system in which Fe: Ir ratio is 1:1 that too with Ir in the $5d^4$ electronic configuration. Another crucial factor is the cation size similarity between Fe^{3+} and Ir^{5+} which results in inter-site cation disorder. In such systems, the degree of disorder can contribute in realization of unusual magnetic ground states. A study conducted by Jordan *et al* (2003) [37] in $BaIr_xFe_{1-x}O_{3-\delta}$ (x = 0.2, 0.3, 0.6) concluded that a small variation in the

chemical environment results in significant variation in the structural and magnetic properties. Compounds with x = 0.2, 0.6 stabilize in the 6H structure with dimers of face shared octahedra separated by corner shared octahedra whereas x = 0.3 stabilizes in the 15R structure. Figure 1.6 shows magnetization measurement of $BaIr_xFe_{1-x}O_{3-\delta}$ (x = 0.2, 0.3, 0.6). Below room temperature, AFM arrangement of FM ordered layers of Fe^{3+} ions gives rise to an AFM ground state. Here, x = 0.2, 0.3 shows anti-ferromagnetic transitions at 220 and 200 K respectively. But, the increase in susceptibility below T_N indicates a disorder in the system. The divergence between ZFC and FC curves is likely to be originating from frustrated interactions of decoupled spins from the magnetic backbone. Both $BaIr_{0.2}Fe_{0.8}O_{3-\delta}$, $BaIr_{0.3}Fe_{0.7}O_{3-\delta}$ undergo a spin glass transition at lower temperatures of 23 K and 50 K, well below T_N. But the third compound $BaIr_{0.6}Fe_{0.4}O_3$ shows a single transition to a spin glass state below 20K. This concludes that as the Ir content increases cation order decreases and long-range order disappears. A very similar compound Sr_2FeIrO_6 exhibits an anti-ferromagnetic transition at 120K and a spin glass transition at around 40K [38]. Significant site disorder was observed in $Ba_3Fe_{1.56}Ir_{1.44}O_9$ [39]. Thus we expect high inter-site disorder in Ba_2FeIrO_6 , which could result in a glassy phase.

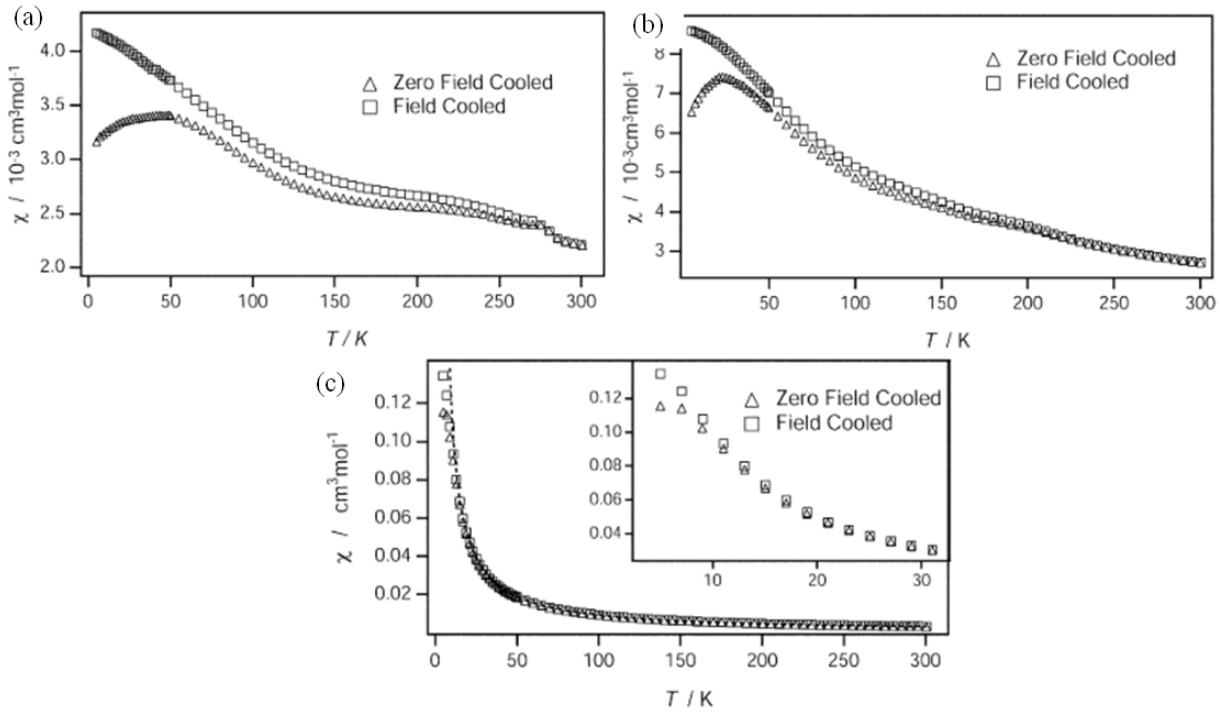

Figure 1.6 Magnetic susceptibility of $BaIr_xFe_{1-x}O_{3-\delta}$ (x= 0.2, 0.3, 0.6) as a function of temperature in an applied field of 100 Oe (a) $BaIr_{0.2}Fe_{0.8}O_{3-\delta}$ (b) $BaIr_{0.3}Fe_{0.7}O_{3-\delta}$ (c) $BaIr_{0.6}Fe_{0.4}O_{3-\delta}$ [37].

1.3.1 Antisite disorder

One feature that makes Double Perovskites different from Perovskites is the disorder in the *B* cation arrangement. It is quantified as a long-range order parameter $S = 2g_B-1$, where g_B is the occupancy of *B* cation at its correct crystallographic site. A completely ordered lattice will have S = 1. Commonly found disorder in *B* cation arrangement is the antisite disorder where *B'* and *B''* cations exchange their positions due to the similarity in their ionic sizes or oxidation states. The disorder is favored if the difference in cation oxidation states $\Delta Z_B = |Z_{B''} - Z_{B'}|$ is less than two considering the balance between electrostatic repulsion and entropy. In terms of difference in ionic radii; $\Delta r_B = |r_{B''}-r_{B'}|$, a difference higher than 0.2Å would result in ordering. An interesting category of Double Perovskites is the ones having $\Delta Z_B = 2$ where disordered, ordered, and partially ordered systems are reported throughout the Δr_B range [3].

1.4 $Y_2(Ni/Co)IrO_6$: Double Perovskites with high magnetic transition temperature

Double Perovskites offer the flexibility to choose different cations for *A* and *B* sites to tune the magnetic as well as electronic ground states. Along with different magnetic *B* cation combinations, one can also add magnetic *A* cations and the best choice would be from lanthanide series considering the relatively large size requirement for *A* site. T. Ferreira *et al* [40] conducted a study on Ln_2MIrO_6 (Ln= La, Pr, Nd, Sm-Gd, M = Mg, Ni), where different combinations of magnetic and non-magnetic cations were used to build a Double Perovskite structure. It turns out that for the Ln_2NiIrO_6 series there is a strong correlation between the *A*-site cation size and the magnetic transition temperature. The series has an ordered rock-salt arrangement with monoclinic structure but has distorted BO_6 octahedra. The smaller size of *A* cation is compensated by bending the Ni-O-Ir bond. Hence, smaller the size of the *A* cation; more the deviation from ideal 180˚ Ni-O-Ir bond angle, and more the distortion in the BO_6 octahedra. Due to the strong AFM interaction between Ni^{2+} and Ir^{4+}, the compounds were reported to exhibit canted anti-ferromagnetism, with the canting angle increasing with octahedral distortion. The reduced Ni-O-Ir bond angle strengthens the interaction and hence the magnetic transition temperature increases from 75K for La to 170K for Gd shown in Figure 1.7. More recently, the high pressure synthesis of the Lu_2NiIrO_6 system was reported in [41], which also follows the same trend. The smallest size of Lu in the Lanthanide series shows up as the highest ordering temperature of 207K for Lu_2NiIrO_6. This series shows the

extent of magneto-structural coupling in 3*d*-5*d* based Double Perovskites where both *B* cations are magnetic and one of them possesses high SOC.

We aim to extend this family by placing Yttrium in the *A*-site. Since the ionic radius of Y^{3+} is between Gd and Lu, we expect a Double Perovskite with magnetic ordering temperature between 170K and 207K. Also, with Yttrium being non-magnetic, this Double Perovskite is likely to be completely free from any influence of 4*f* magnetism, which is a factor in many of the Lanthnaoids. Concerning the electron correlation in the system, it is a good playground to study the interactions between a 3*d* *A*-cation and 3*d*-5*d* *B*-cations. We aim to study the extent of magneto-structural coupling in a 3*d*-5*d* system with high SOC. Along with this, to see how a change in *B* cation would affect the magneto-structural coupling and the transition temperature, we have tried to synthesize and study the physical properties of Y_2CoIrO_6 as well.

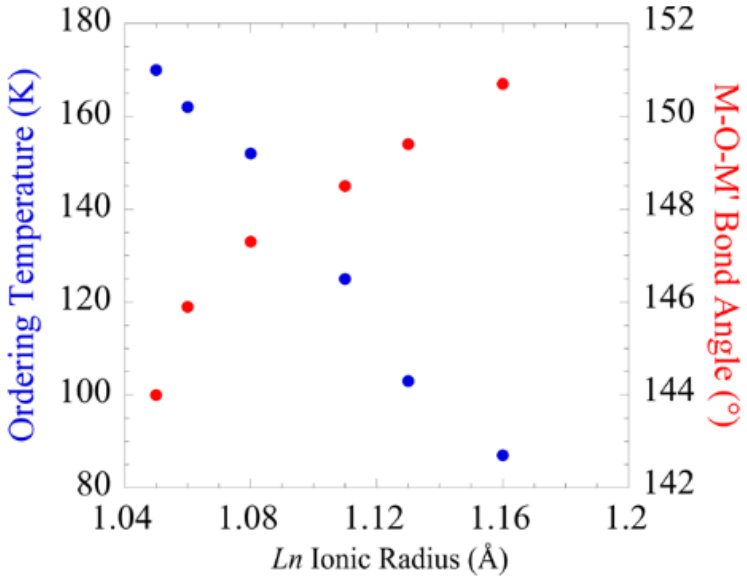

Figure 1.7 Ionic radii dependence of ordering temperature and M-O-M' bond angle [40].

1.4.1 Octahedral tilt

As mentioned earlier, an ideal Perovskite has a cubic structure. But non-ideal situations lead to cation displacement, distortions or tilt in BO_6 octahedra. Among this, the most common occurrence is the tilting of octahedra to accommodate smaller *A* cations. Such tilting can be described by Glazer's notation [42]. There are 12 possible tilt systems for rock salt ordered Double Perovskites and seven of them favor double perovskite with a single *A* cation. In a Glazer notation, there are two terms: one which describes the magnitude of rotation about an axis relative to rotations about other axes. The superscript indicates the direction of rotation

relative to the adjacent layer. For example in $a^-a^-b^+$, the rotation angle about the z-axis is different from that about other two axes. Similarly, in x and y tilt axes, rotations of two adjacent octahedra are in opposite directions indicated by negative superscript. For each tilt system, a space group is assigned. Commonly observed tilt systems in rock salt ordered Double Perovskite as a function of decreasing tolerance factor: $a^0a^0a^0$ (*Fm-3m*) → $a^0a^0c^-$ (*I4/m*) or $a^-a^-a^-$ (*R*-3) →$a^0b^-b^-$ (*I2/m*) →$a^-a^-c^+$(*P2₁/n*) [3]. Monoclinic distortions are preferred for t<0.97 which is observed in Ln_2NiIrO_6.

1.5 Plan of the thesis

Due to the intricate interplay of SOC, on-site Coulombic interaction and crystal field energy, Iridium based Double Perovskites are the sources of novel quantum materials. The aim of this thesis is to synthesize polycrystalline Ba_2FeIrO_6, Y_2NiIrO_6, and Y_2CoIrO_6 via a solid-state route where the former one has Ir in $5d^4$ configuration while the other two have $5d^5$ configuration. Phase confirmation and structural study has been done using Rietveld refinement of room temperature lab XRD. Magnetic and transport measurements need to be done for a detailed structure-property study of these new samples.

Chapter 2 Experimental methods

2.1 Synthesis

All compounds were synthesized by solid-state ceramic route in which appropriate chemicals; oxides, carbonates, or metals of the respective elements were mixed stoichiometrically and thoroughly using an agate mortar and pestle. Since the reaction does not happen through any solvent, the reagent mixture has to be very homogeneous and should be given high enough temperatures and time to allow diffusion of reactants. But these high temperatures should not cause volatilization or melting of the reagents. A thorough grinding with 99.99% Ethanol is required to ensure the homogeneity of the reagent mixture at the molecular level while the high-temperature sintering facilitates the homogeneity at the atomic level. Hygroscopic reagents need to be preheated before weighing. Reactive chemicals, fine-sized homogenous particles, pelletization, intermediate grinding, gas environment, etc enhance the reactivity. Depending upon the synthesis procedure, sintering temperature and even the stoichiometry of the product can vary. PID controlled programmable furnaces were used for the reaction and after each sintering, Powder X-ray Diffraction (PXRD) and Energy Dispersive X-ray Spectroscopy (EDX) have been carried out on the sample.

2.1.1 Synthesis of Ba_2FeIrO_6

The synthesis was done by the solid-state method. Stoichiometric amounts of preheated $BaCO_3$, Ir metal powder, and Fe_2O_3 were ground well in a mortar and pestle using 99.99% ethanol. The amount of sample prepared in bulk was 4 gm. The reaction was carried out in a tube furnace according to profiles given in Table 2.1. The balanced equation is as follows:

$$4BaCO_3 + Fe_2O_3 + 2Ir + 5/2\ O_2 \rightarrow 2Ba_2FeIrO_6 + 4CO_2$$

Treatments	Temp (˚c) / Time	Environment, ramp rate
T1	900/24Hrs	O_2, 1.4˚/min
T2	1000/ 48Hrs	
T3	1000/ 72Hrs	

Table 2.1 Temperature treatments given to Ba_2FeIrO_6

2.1.2 Synthesis of Y_2NiIrO_6

The synthesis was done by the solid-state method. Stoichiometric amounts of preheated Y_2O_3, Ir metal powder, and NiO were ground well in a mortar and pestle using 99.99% ethanol. The amount of sample prepared in bulk was 4 gm. The reaction was carried out in a Nabertherm Box furnace according to profiles given in Table 2.2. All the heat treatments except the first ones were done in pellet form. The balanced equation is as follows:

$$Y_2O_3 + NiO + Ir + O_2 \rightarrow Y_2NiIrO_6$$

Compound	Heat treatments	Furnace type, Environment, Total time, ramp rate
Y_2NiIrO_6	12 short heat treatments were given at 1200˚C	Bigbox furnace, air, 113Hrs, 20˚/ min

Table 2.2 Temperature treatments given to Y_2NiIrO_6

In terms of synthesis temperature, this compound has a very narrow stability regime. At temperatures lower than 1200˚C, the system forms the Pyrochlore phase whereas longer treatments at 1200˚C or treatments at a higher temperature result in the decomposition of the Double Perovskite phase. Also, the volatile nature of Ir and NiO makes the synthesis non-trivial. Four trials have been done to standardize the synthesis procedure.

2.1.2 Synthesis of Y_2CoIrO_6

Multiple trials have been done to synthesis Y_2CoIrO_6, but we were unable to form a good quality single phase specimen. All the synthesis procedures followed are discussed in Chapter 3 of this thesis.

Other than these compounds, syntheses of Y_2CoIrO_7 and Y_2CuIrO_7 have also been attempted. But trials did not result in a single phase.

2.2 X-Ray Diffraction (XRD)

X-ray diffraction techniques were used for phase confirmation of the samples after each sintering. XRD is the elastic scattering of X-rays from the atoms in a crystalline sample. Constructive interference between the scattered rays from the atoms in parallel lattice planes gives peaks in the XRD profile. They follow Bragg's law of diffraction; $2d\sin\theta = n\lambda$, where d is the spacing between consecutive planes, θ is the angle of diffraction, λ is the wavelength and n is an integer. For each compound, d-spacing between particular planes is different;

hence angle at which the peak appears for different planes will also be different. Thus, an XRD pattern is a fingerprint of a material. Bruker D8 Advance Powder X-ray Diffractometer facility at IISER Pune was used for phase confirmation of the samples after each sintering. It has Bragg-Brentano geometry where the source and the detector can move in the entire 2θ range but the sample orientation is fixed. It produces Cu K_α X-rays of wavelength 0.15406 nm. For measurement, the polycrystalline sample needs to be well ground to ensure random orientation of crystalline planes. The output of the diffraction i.e. intensity *vs* 2θ was recorded electronically and International Centre for Diffraction Data (ICSD) was used for primary analysis of the XRD profile.

2.3 Structural Analysis

Structural analyses of the reported compounds have been done using the Rietveld refinement method [43]. It is a least-square refinement method where, in each iteration, the program tries to minimize the residual S_y:

$$S_y = \sum_i w_i(y_i - y_{ci}) \quad \text{Where,}$$

y_i = Measured intensity in i^{th} step

y_{ci}= Calculated intensity in i^{th} step

$w_i=1/y_i$

Calculated intensity y_{ci} of a particular Bragg reflection depends on the square of the structure factor F_K.

$$F_K = \sum_j N_j f_j \exp\left[2\pi i\left(hx_j + ky_j + lz_j\right)\right] \exp\left(-8\pi^2 u_s^2 \sin^2\theta / \lambda^2\right)$$

Where h, k, l = Miller indices of a Bragg reflection

x_j, y_j, z_j = Atomic positional parameters of the j^{th} atom

N_j = site occupancy multiplier for j^{th} atom

f_j= Atomic form factor of the jth atom

u_s^2 is the root mean square value of thermal displacement of the jth atom in direction s parallel to the diffraction vector

The intensity at the ith step is calculated from $|F_K|^2$values of given structural model and background intensity at the ith position.

$$y_{ci} = S \sum_k L_k |F_k|^2 \phi(2\theta_i - 2\theta_k) P_k A + y_{bi}$$

S = Scale factor

K = Miller indices h, k, l for a Bragg reflection

L_k = Lorentz polarization and multiplicity factor

ϕ = Bragg reflection profile function

P_k = Preferred orientation function

A = Absorption factor

F_k= Structure factor for kth Bragg reflection

y_{bi}= Background intensity at ith step

Since the residual function is non-linear, the solution must be found by an iterative procedure. Also, the program needs a good starting model otherwise it will lead to divergence of the function or to a local minimum. The reflection profile function ϕ considers the effects of both instrumental and specimen features. For intensity *vs* 2θ data, the breadth H of a Bragg reflection, Full-Width-at-Half-Maxima is given by,

$$H^2 = u \tan^2 \theta + v \tan \theta + w$$

Where u, v, w are refinable parameters.

The quality of the fit is given by R values. It indicates the progress of the refinement after each iteration and gives the goodness of fit as well. Among several R values that users have developed, R_{wp} is the most reliable one as its numerator is the residual function that is being minimized in each iteration.

$$R_{wp} = \left[\frac{\sum w_i (y_i(obs) - y_i(cal))^2}{\sum w_i (y_i(obs))^2} \right]^{\frac{1}{2}}$$

Another criterion of fit is the 'goodness of fit', S which is given by,

$$S = \frac{R_{wp}}{R_e}$$

Where R_e is the R- expected defined by

$$R_e = \left[\frac{N - P}{\sum w_i (y_i(obs))^2}\right]^2$$

A goodness fit close to 1.3 is considered to be the best fit. Any value much less than or much higher than this value indicates issues in the refinement. Rietveld refinement is a very useful method to extract data from the XRD pattern of a specimen. This method can also be extended for solving magnetic structures using Neutron diffraction data. FullProf software was used for the Rietveld refinement.

2.4 Field Emission Scanning Electron Microscopy (FESEM) & Energy Dispersive X-ray Spectroscopy (EDXS)

Field Emission Scanning Electron Microscopy (FESEM) provides high-resolution topographical features of a specimen. Electrons released from field emission source are accelerated through a high electric field gradient. These electrons are focused and bombarded on the specimen resulting in the release of secondary electrons from each spot on the specimen. The angle and velocity of secondary electrons relate to the morphology of the sample. The detector catches these secondary electrons, amplifies and transforms into a 3-D image.

Energy Dispersive X-ray Spectroscopy (EDXS) technique is used to find the elemental composition in a sample. EDXS systems are attached to SEM instruments where microscopy facility helps to focus on the area of interest on the specimen. The sample is bombarded with high energy electrons, resulting in the release of an electron from the inner shell of an atom. An electron from higher energy level replaces the hole created and this results in the release of X-rays. The detector converts the individual X-rays into electric voltage and the composition is determined from this integrated intensity of each peak, given each element in the periodic table has a characteristic line energy.

2.5 Heat capacity Measurement

Heat capacity measurements were done using the Physical Property Measurement System (PPMS) (Quantum Design) facility at TIFR, Mumbai. The measurements were carried out in 2-300 K range on a puck based micro-calorimeter (Figure 2.1)

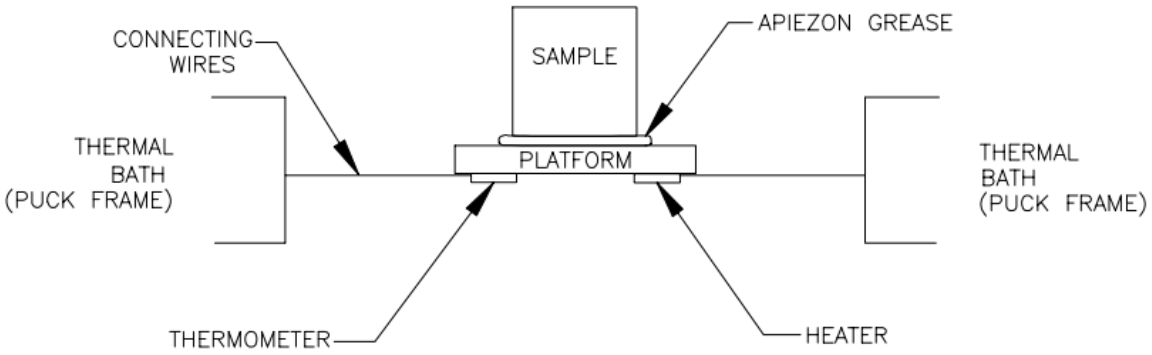

Figure 2.1 Sample platform in PPMS heat capacity probe [44]

A heater and thermometer are attached to the bottom side of the sample platform and to ensure good thermal contact Apiezon N grease is used in between sample and addenda. To avoid any heat loss, a high vacuum is maintained throughout the measurement. Apparatus measures the specific heat capacity at constant pressure, $C_P = \left(\frac{dQ}{dT}\right)_P$ by relaxation technique. Here the sample holder is given a thermal pulse for a constant time and upon removing it, sample temperature exponentially decays to bath temperature. Heat capacity is measured from this decay rate. The heat capacity of the sample alone is calculated by subtracting the contribution from addenda with grease from the total heat capacity. Heat capacity measurements reported in this thesis were carried out on samples of the approximate weight of 6mg. These measurements give information about lattice, electronic and magnetic properties of the specimen.

Chapter 3 Results and discussion

3.1 Ba_2FeIrO_6

The sample was synthesized in the third sintering itself (Table 2.1). Further heat treatments given to a part of the bulk sample at 1100˚C did not result in any change in the XRD pattern. Figure 3.1 shows SEM images of nano-size, layered hexagonal facets of the sample. EDXS data confirms 2:1:1 ratio between Ba:Fe:Ir. Figure 3.2 is a comparison of lab XRD of Ba_2FeIrO_6 after third sintering with reported $BaIr_{0.6}Fe_{0.4}O_3$ [37]

3.1.1 Structural analysis

Structural refinement of the lab XRD taken at room temperature was done by the Rietveld method using the Fullprof software. Figure 3.3 shows refinement fit for powder XRD pattern of Ba_2FeIrO_6 and .Table 3.1 lists the lattice parameters obtained from refinement. Table 3.2 lists the atomic positions and the fractional occupancy of each site. Refinement without adding anti-site disorder in both the *B* cation site did not yield a good fit, in fact for multiple peaks; there were huge intensity differences between calculated and observed peaks. Also, along with FWHM parameters, refinement of shape parameter and asymmetry parameters were necessary to match the observed and generated peaks throughout the 2θ range. Pseudo-Voigt was chosen as the peak shape model and background was generated by linear interpolation between a set of points.

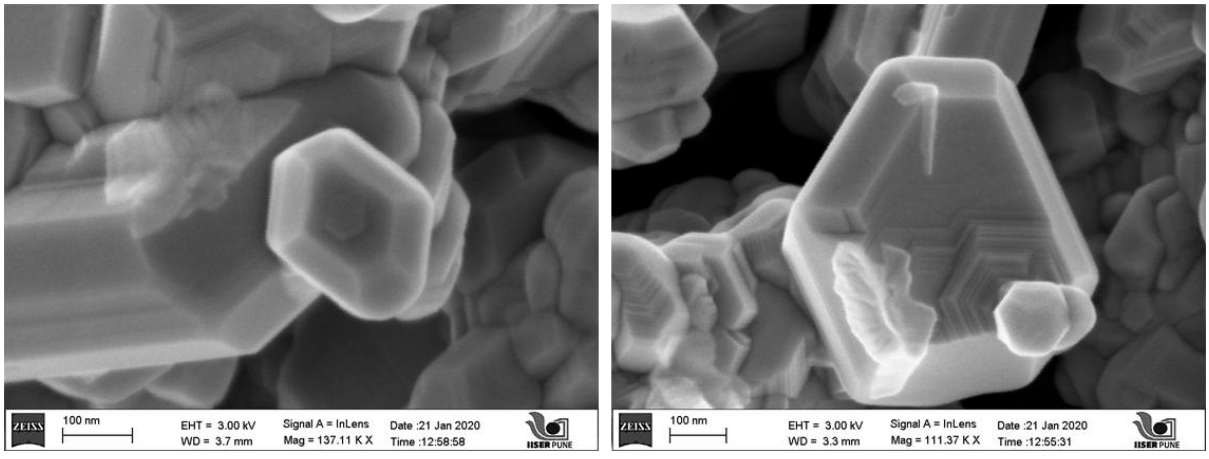

Figure 3.1 Nano-size, layered hexagonal facets of Ba_2FeIrO_6

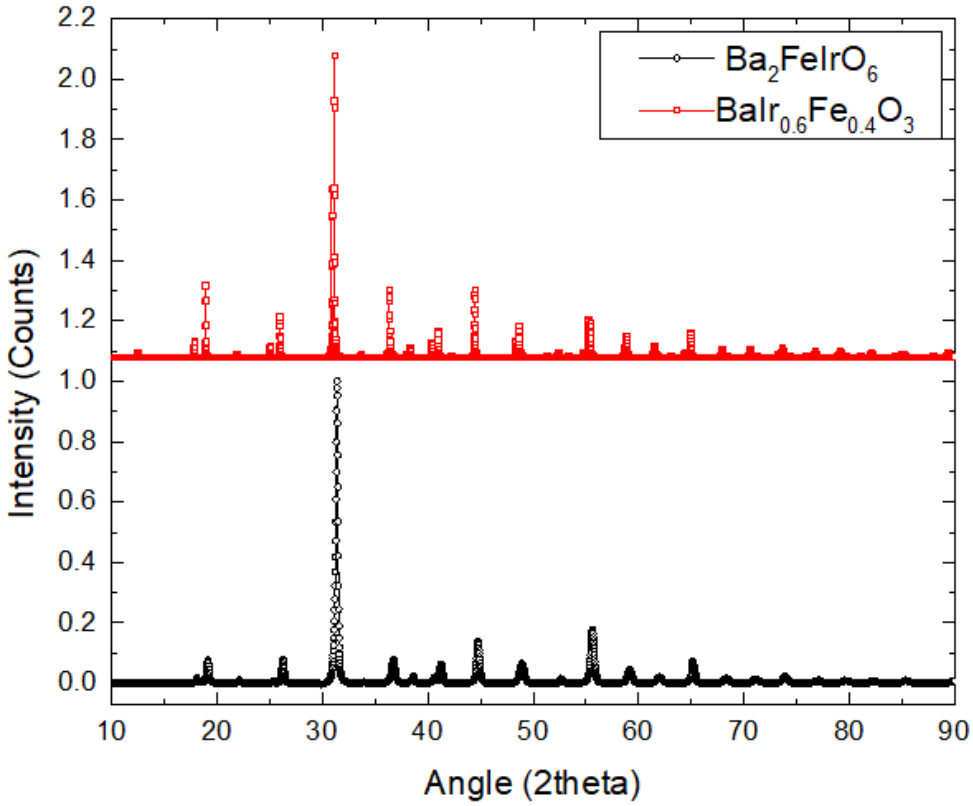

Figure 3.2 A comparison of lab XRD of Ba_2FeIrO_6 (black) after third sintering with reported $BaIr_{0.6}Fe_{0.4}O_3$ (red)

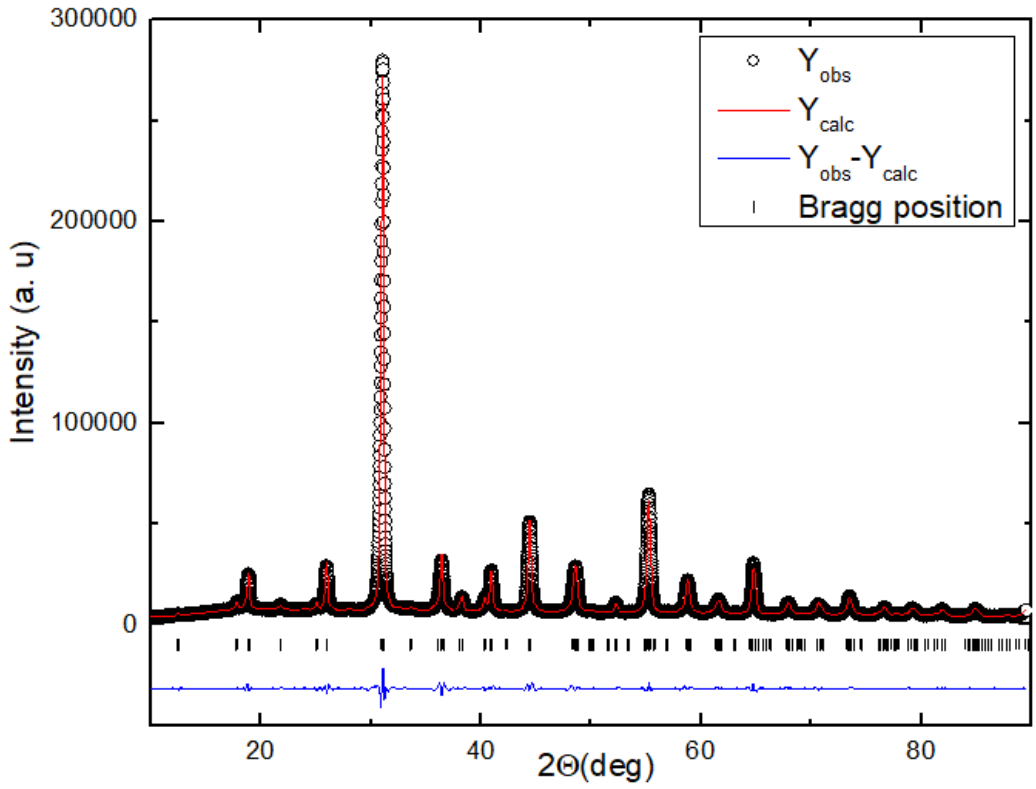

Figure 3.3 Rietveld refinement fit for Ba_2FeIrO_6.

Chemical formula	Ba_2FeIrO_6
Molecular weight, g/mol	618.71
Temperature, K	296
Crystal structure	Hexagonal
Space group symmetry and number	*$P6_3/mmc$*, 194
Unit cell parameters	
a, b (A˚)	5.7556
c (A˚)	14.1992
α, β (deg)	90
γ (deg)	120
Volume ($A^{\circ 3}$)	470.3759
Diffraction angle range (θ deg)	10-90
Step size (θ deg)	0.01
R values	
R_{wp}	7.66
R_e	2.12
Chi^2	13
Goodness of fit (R_{wp}/R_e)	3.6

.**Table 3.1** Lattice and fitting parameters of Ba_2FeIrO_6 obtained from Rietveld refinement.

Atom	x/a	y/b	z/c	Fractional occupancy
Ba1	0	0	0.25	1
Ba2	0.33333	0.66667	0.09078	1
Fe1	0	0	0	0.80964
Ir1	0	0	0	0.19044
Fe2	0.33333	0.66667	0.84477	0.40434
Ir2	0.33333	0.66667	0.84477	0.59562
O1	0.49598	-0.49598	0.25	1
O2	0.84838	-0.84838	0.08568	1

Table 3.2 Refined atomic positions and fractional occupancy.

3.1.2 Specific heat measurement of Ba_2FeIrO_6

Molar heat capacity as a function of temperature (Figure 3.4) does not show any clear anomaly in the temperature range 3-300K which indicates there is no long-range order in the system within this temperature range. Also, C_P/T^3 vs T (Figure 3.5) shows an upturn at a lower temperature. Both these features corroborate the presence of a glassy phase [45]. A proper linear fit of the plot C_p/T vs T^2 (Figure 3.6) at low temperatures asserts that the compound follows Debye's formula of specific heat. Debye parameters were calculated from a linear fit between the 10-26K range. Deviation from the linear fit, C_p/T vs T^2 below 10K is likely from the significant antisite disorder in the system.

$$\text{From the linear fit } Cp/T = \gamma + \beta T^2$$

Sommerfield coefficient γ=67.99082 mJ/mole-K/K, β= 0.66349 mJ/mole-K/K^3

$$\text{Debye temperature } \theta = \left(\frac{12\pi^4 PR}{5\beta}\right)^{1/3}$$

Calculated Debye temperature for Ba_2FeIrO_6 is 308K

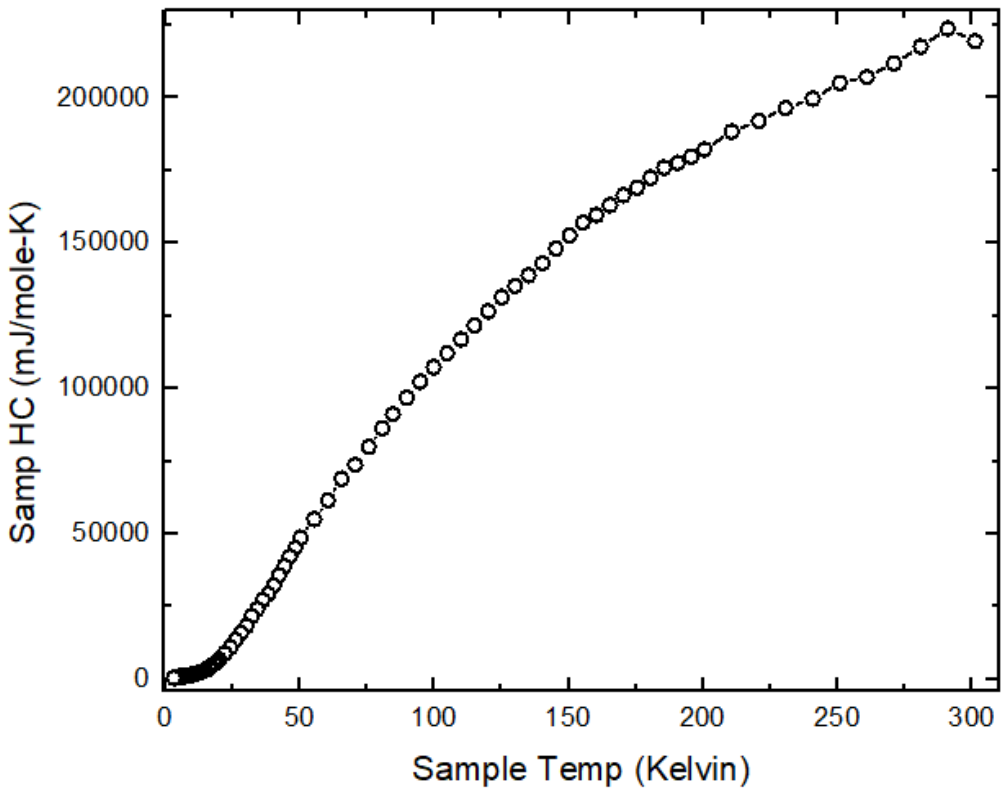

Figure 3.4 Molar heat capacity of Ba_2FeIrO_6 as a function of temperature

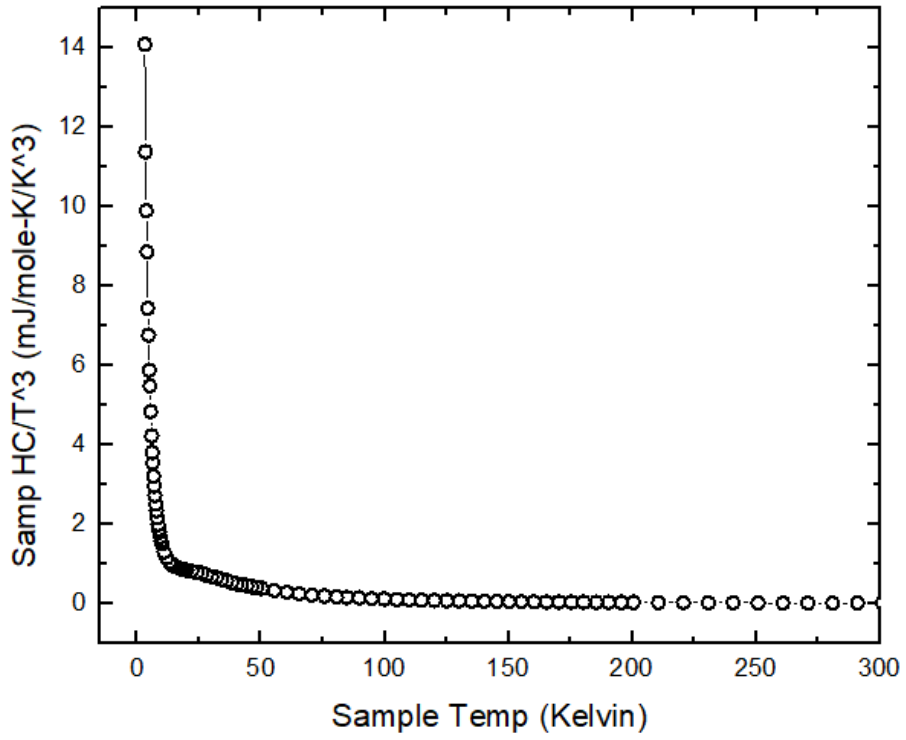

Figure 3.5 C_P/T^3 vs T plot of molar heat capacity

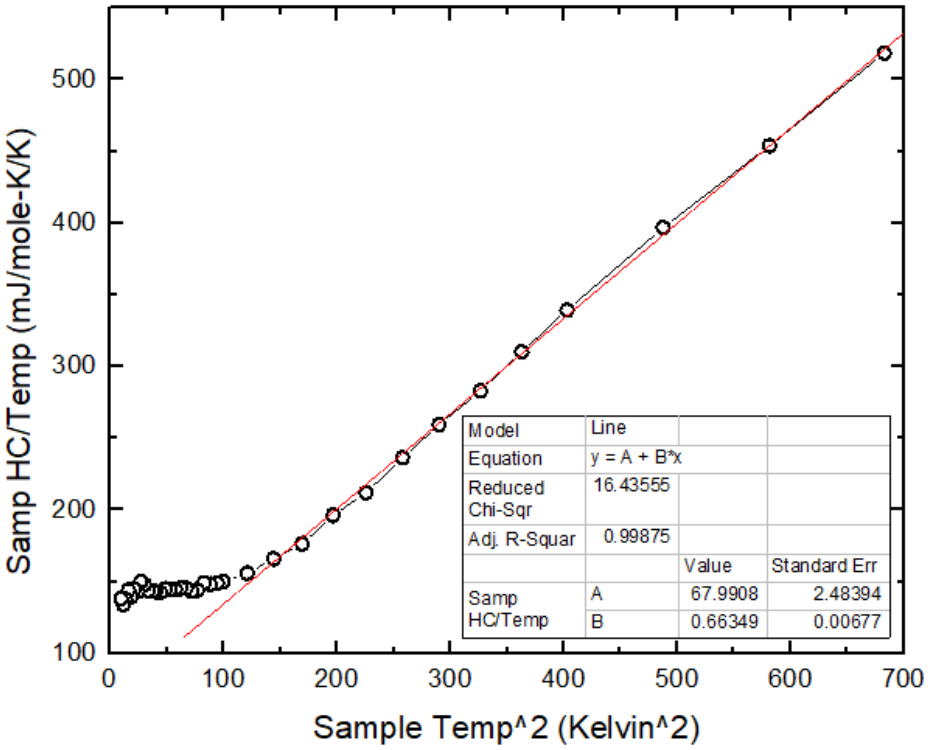

Figure 3.6 Linear fit of C_p/T vs T^2 in the temperature range 10-26K

3.2 Y_2NiIrO_6

3.2.1 Synthesis considerations

Multiple trials have been conducted to standardize the synthesis procedure for Y_2NiIrO_6. All sinterings were carried out in a Nabertherm high-temperature furnace in air. Figure 3.7 shows the temperature sequence of Trial1 in which 300 mg of sample synthesis was attempted. The temperature ramp rate was 1.5˚C/min and IrO_2 was used as a reagent. Even though the target phase formed at 1200˚C, some amount of Y_2O_3 and NiO were still present. This can happen if raw materials were mixed non-stoichiometrically or the reaction is incomplete. Since the XRD of precursor material IrO_2 showed Ir metal content as well, synthesis of a new batch; Trial2 was started. The increased intensity of Y_2O_3 and NiO in subsequent heat treatments of the Trial1 also indicated decomposition of the primary phase. The absence of any Ir peak is attributable to its volatility.

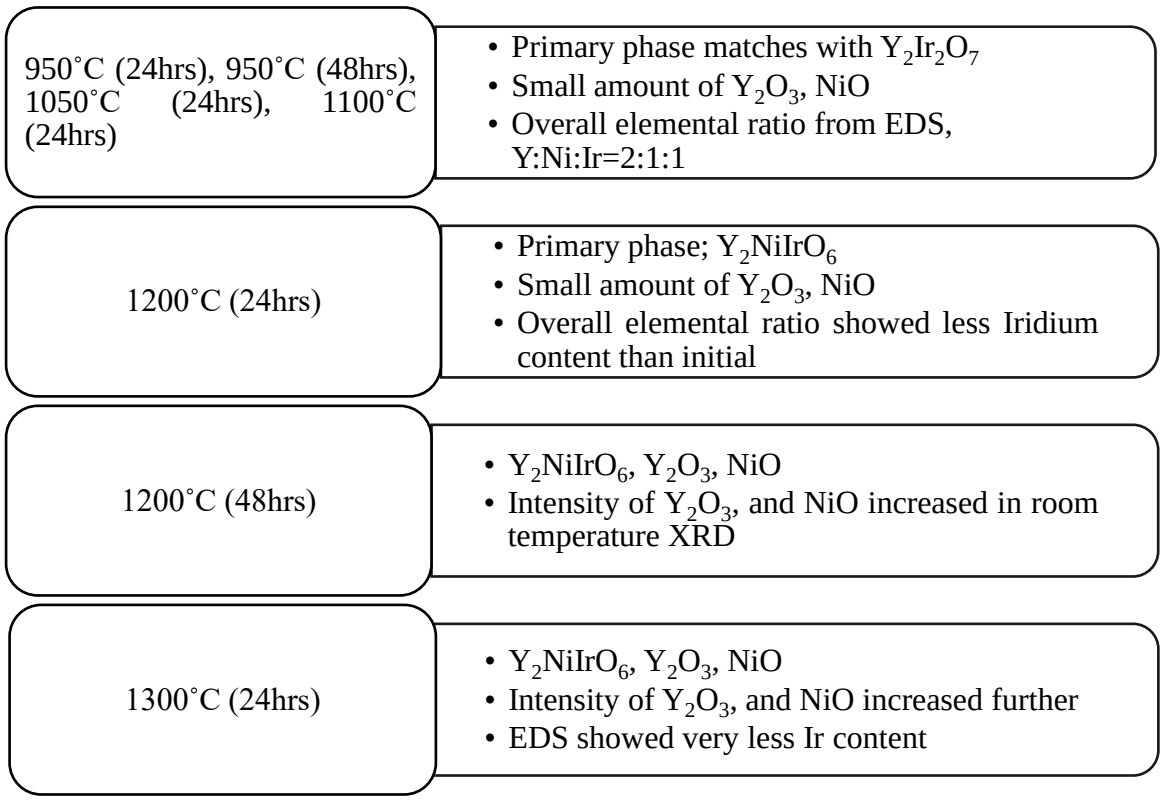

Figure 3.7 Temperature sequence given to Y_2NiIrO_6 Trial1 and results of each sintering

In the second trial (Figure 3.8), Ir metal powder was used as raw material and the temperature ramp rate was increased to 2.5˚C/min. Since, this also followed the same trend as in Trial1, it was concluded that the problem was not from the Ir reagent. It is noticeable that at 1200˚C Y_2NiIrO_6 starts forming and the $Y_2Ir_2O_7$ phase decomposes. But a long time at the said

temperature (even 24 hr duration) results in Iridium losses from the system leaving unreacted Y_2O_3 and NiO. Considering this, a third trial was carried out with 5% excess Iridium with respect to the balanced equation. To avoid Pyrochlore phase formation in the temperature range 950˚C-1100˚C, ramp rate was kept as 10˚/min. This also gave a similar quantity of Y_2O_3 and NiO but along with Ir metal. The synthesis procedure for Trial3 is shown in Figure 3.9.

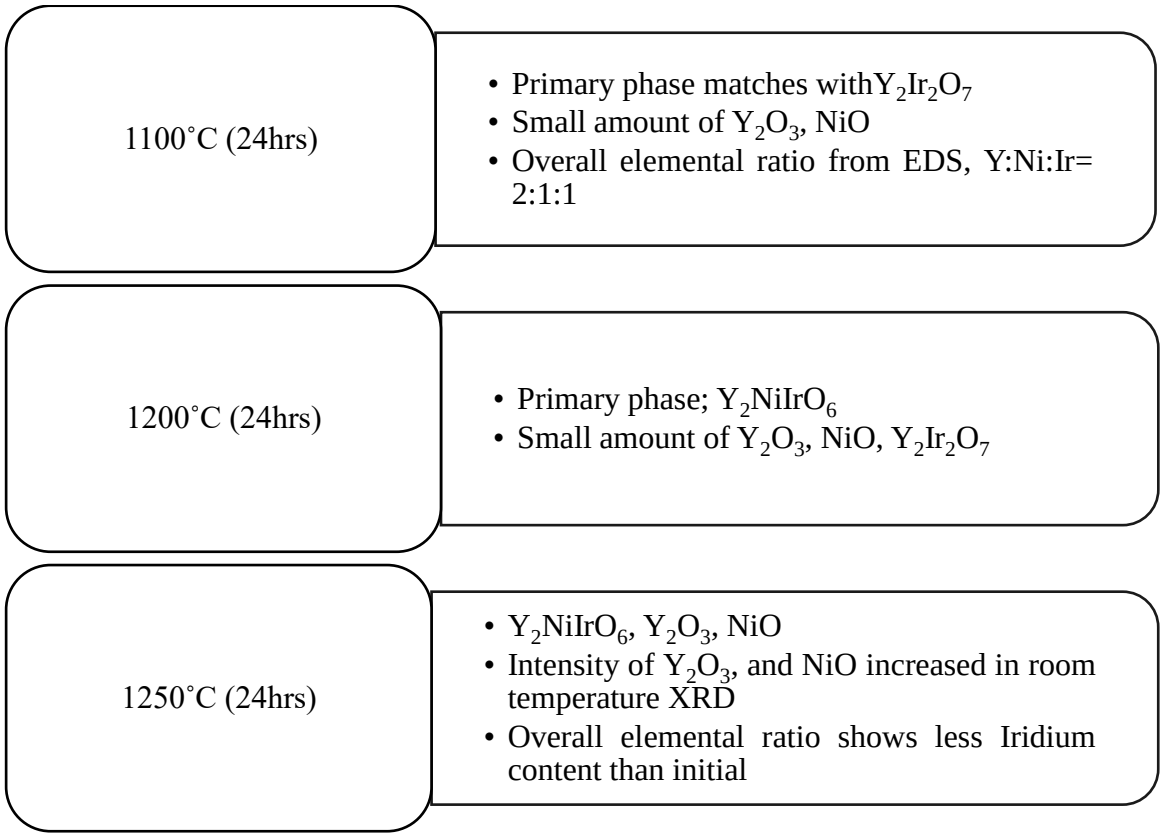

Figure 3.8 Temperature sequence given to Y_2NiIrO_6 trial2 and results of each sintering

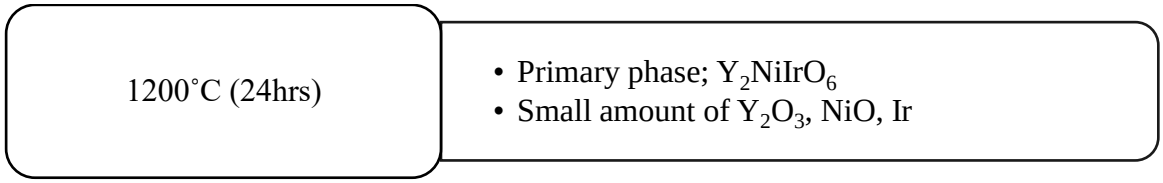

Figure 3.9 Temperature sequence given to Y_2NiIrO_6 trial3 and results of each sintering

From all three trials, the following points are clear;

- Y_2NiIrO_6 formation temperature is 1200˚C
- At any lower temperature, Pyrochore phase $Y_2Ir_2O_7$ is stable and this phase decomposes at 1200˚C
- Longer heat treatments at 1200˚C or at any higher temperature results in decomposition of Y_2NiIrO_6
- A fast ramping rate would help to avoid the formation of Pyrochlore phase

Following these points, in Trial4 200 mg of sample was given short treatments at 1200˚C with a ramp rate of 20˚/min. After the second heat treatment, the sample was left with small amounts of Y_2O_3, NiO, IrO_2. But their quantity reduced in each subsequent sintering. Finally, after the eighth sintering, a single phase of Y_2NiIrO_6 was obtained. Figure 3.11 shows the sintering sequence for Trial4 and Figure 3.10 shows a decrease in raw material content after each treatment. Primary peak intensity of each of these raw materials were monitored for this analysis. A slightly higher content of NiO in the plot is due to the coincidence of NiO primary peak with a peak of Y_2NiIrO_6.

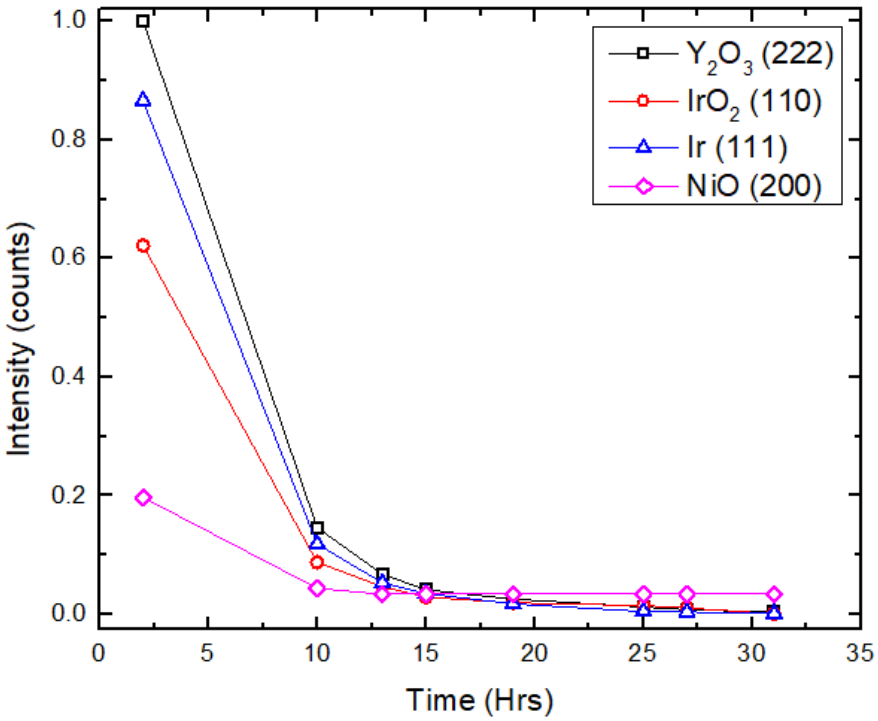

Figure 3.10 Decrease in primary peak intensity of raw materials after each sintering is plotted as a function of time. Miller indices of respective peaks are labelled in the graph.

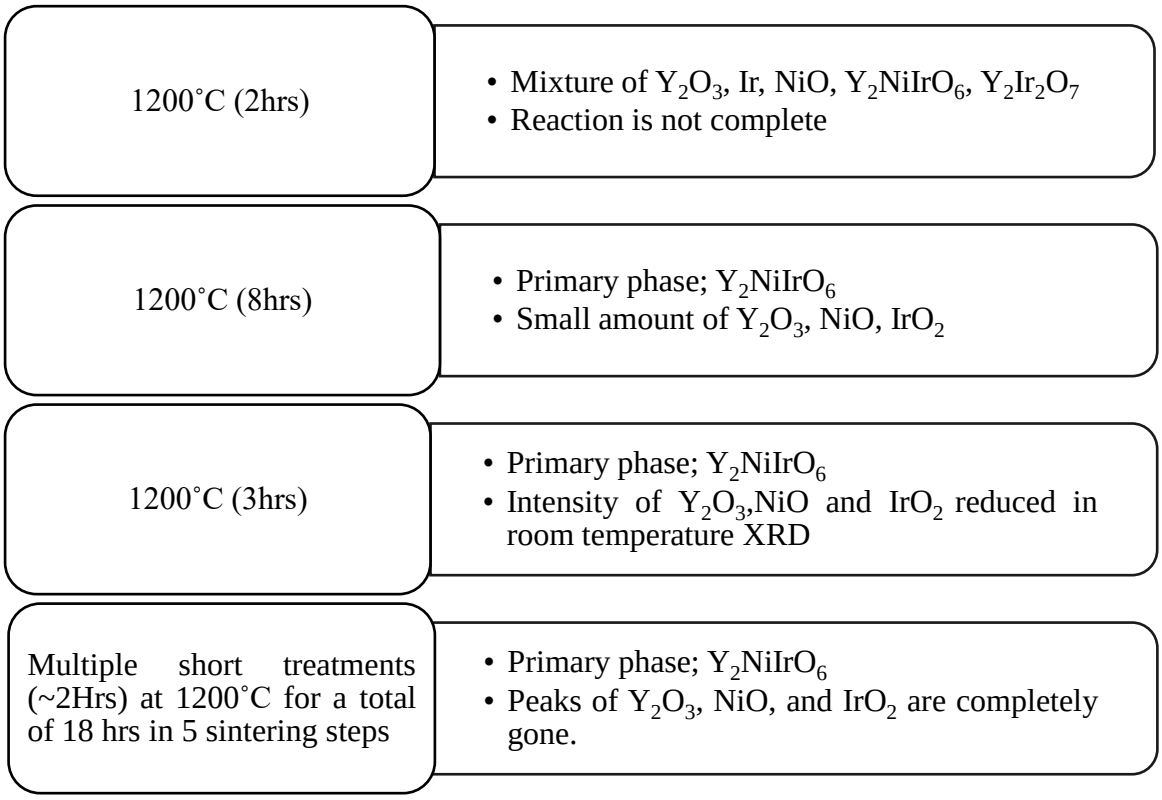

Figure 3.11 Temperature sequence given to Y_2NiIrO_6 trial4 and results of each sintering

Bulk synthesis (4gm) of Y_2NiIrO_6 was started immediately after Trial4. Here except the first two treatments, reactions were carried out in pellet form made using 13 mm die in KBr press. Table 2.2 presents the temperature profile of the bulk sample and Figure 3.12 shows a gradual decrease in Y_2O_3, NiO, IrO_2 content with sintering time. The slow reaction rate of bulk compared to Trial4 could be due to slow oxidation of Ir into IrO_2 and hence bulk synthesis took longer sintering time than the trial sample. The reaction was performed in the Nabertherm big box furnace in air. A very little amount of oxygen airflow would have increased the reaction rate as bulk quantity needed more oxygen than 200mg of trial. Twelve heat treatments at 1200˚ resulted in approximately 3% loss of both Ir and NiO from the system, leaving 6% unreacted Y_2O_3 in the end. The primary peak of Y_2O_3, (222), appears at 29.4˚ in the XRD pattern (Figure 3.13). Since, Y^{3+} is non-magnetic this would not be a problem in magnetization measurements. It is observed that similar reported compounds were synthesized in other methods such as flux growth, high pressure method, etc. which reduced the synthesis temperature considerably and avoided any reagent loss from the system at high temperatures [41, 46-49]. Hence, they could achieve a single phase. But wherever the solid-state method was chosen, the final product is a mixed-phase with Double Perovskite and some other oxides of reagents [50-53]. The room temperature XRD pattern of Y_2NiIrO_6 has

plotted along with the calculated pattern of Gd_2NiIrO_6 in Figure 3.13. Elemental mapping by EDS shows 1:1 ratio between Ni and Ir while 2.22:1 between Y and Ni/Ir confirming Ni and Ir loss from the system. Ni leaves a stain on the alumina crucible and on the lid as well, which physically indicates this loss.

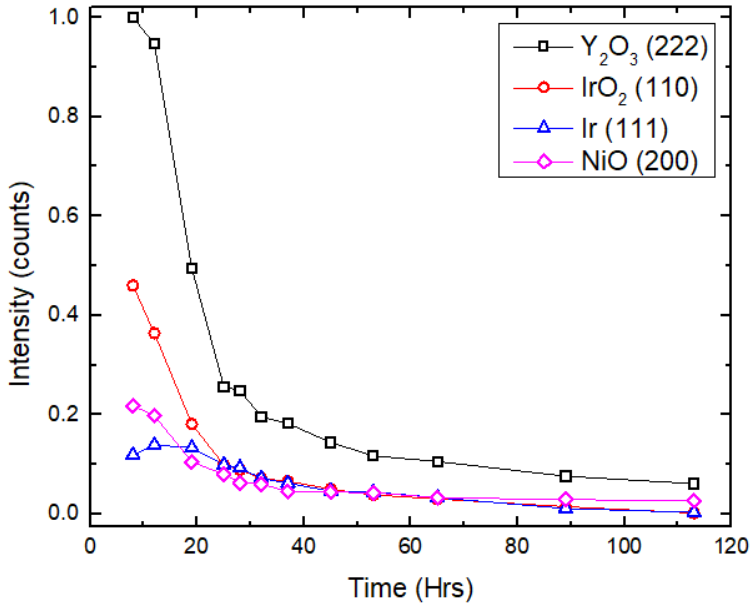

Figure 3.12 Decrease in primary peak intensity of raw materials after each sintering is plotted as a function of time. Miller indices of respective peaks are labelled in the graph.

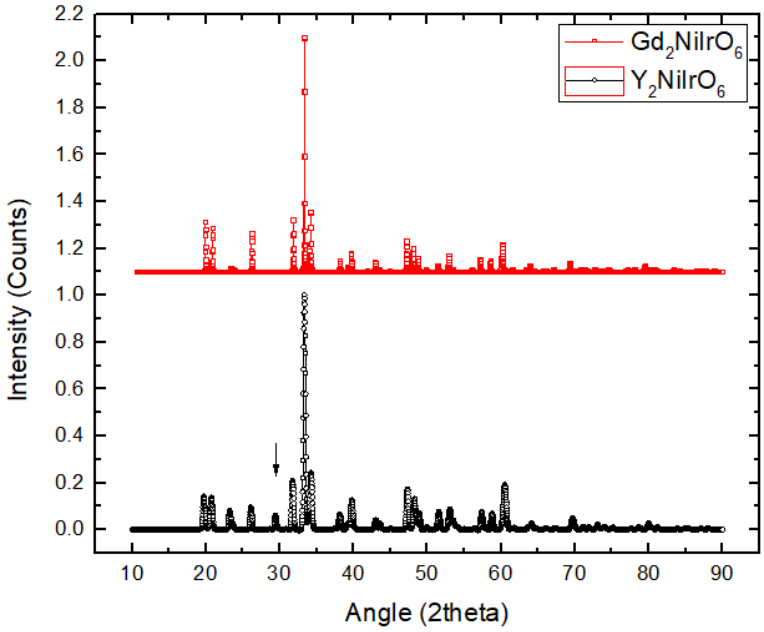

Figure 3.13 A comparison of lab XRD of Y_2NiIrO_6 (black) after twelth sintering with reported Gd_2NiIrO_6 (red). Gd_2NiIrO_6 peak positions are X-shifted for comparison. The arrow mark points to the primary peak of Y_2O_3, (222).

3.2.2 Le-Bail fitting

Le-Bail fitting was done using Lu_2NiIrO_6 as the reference pattern and Table 3.3 lists the lattice parameters obtained from the fit. The structural refinement of this sample is ongoing.

Chemical formula	Y_2NiIrO_6
Molecular weight, g/mol	524.716
Temperature, K	296
Crystal structure	Monoclinic
Space group symmetry and number	$P2_1/n$, 14
Unit cell parameters	
a (A˚)	5.2643
b (A˚)	5.6718
c (A˚)	7.5798
α, γ (deg)	90
β (deg)	90.060
Volume ($A^{\circ 3}$)	226.3181
Diffraction angle range (θ deg)	10-90
Step size (θ deg)	0.02
R values	
R_{wp}	6.75
R_e	1.02
Goodness of fit (R_{wp}/R_e)	6.61

Table 3.3 Lattice parameters of Y_2NiIrO_6 obtained from Le-Bbail fit

Y_2NiIrO_6 crystallizes in a monoclinic structure with space group $P2_1/n$. The unit cell parameters are related to a_p (unit cell edge of a simple cube ABO_3) as $a \approx \sqrt{2}a_p, b \approx \sqrt{2}a_p, c \approx 2a_p, \beta \approx 90°$, expected for the tilt system $a^-a^-b^+$ [54]. Like other compounds of this series [40-41], lattice parameters of Y_2NiIrO_6 are also affected by the octahedral tilting. Variation in lattice parameters with the ionic radius of *A* cation is shown in Figure 3.14. The *a* and *c* edges decrease monotonically with *A* cation size while *b* increases slightly and then decreases with A^{3+} ionic radius. The Glazer tilt system, $a^-a^-b^+$, observed in this series, causes

minimal modifications to the *b* parameter. As the *A* cation radius reduces, deviation of Ni-O-Ir bond angle from 180˚ increases; consequently, the β angle of the monoclinic structure increases except in the case of La_2NiIrO_6. Hence β can be considered as a measure of distortion in the octahedra [46]. In Figure 3.14, the triangular symbol represents lattice parameters and volume of Y_2NiIrO_6. As shown in the figure, Y_2NiIrO_6 fits well into the Ln_2NiIrO_6 series. The decrease in unit cell volume accounts for the decrease in *A* cation size.

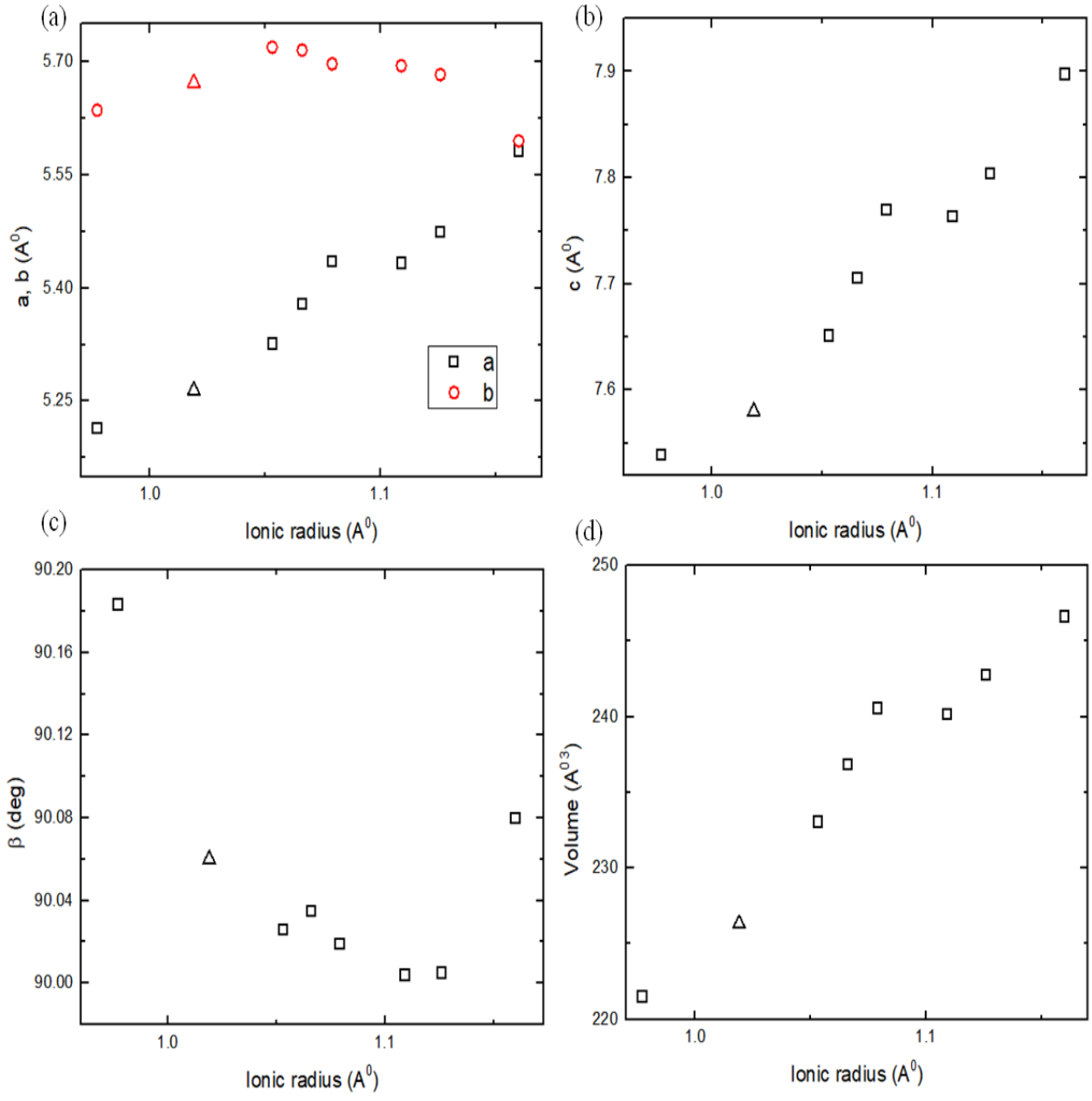

Figure 3.14 Variation of lattice parameters and volume with *A* cation size is shown for the series $(Ln/Y)_2NiIrO_6$, where Ln= La, Pr, Nd, Sm, Eu, Gd, Lu in the descending order of the ionic size. The triangular symbol represents the parameters of Y_2NiIrO_6.

3.2.3 Specific heat measurement

Molar heat capacity as a function of temperature shows an anomaly at 186K as shown in Figure 3.15 indicating the expected magnetic transition in the temperature regime 170-207K. C_P/T^3 vs T in Figure 3.16 shows an upturn at low temperature which is characteristics of a glassy material [45]. To confirm the presence of the glassy phase, C_p/T vs T^2 was plotted (Figure 3.17), which varies linearly below 10K, indicating there is only short-range interactions present in the system at the low-temperature regime.

From the linear fit, $Cp/T = \gamma + \beta T^2$

Sommerfield coefficient γ=2.08056 mJ/mole-K/K, β= 0.23814 mJ/mole-K/K^3

Debye temperature $\theta = \left(\frac{12\pi^4 PR}{5\beta}\right)^{1/3}$

The calculated Debye temperature for Y_2NiIrO_6 is 433K.

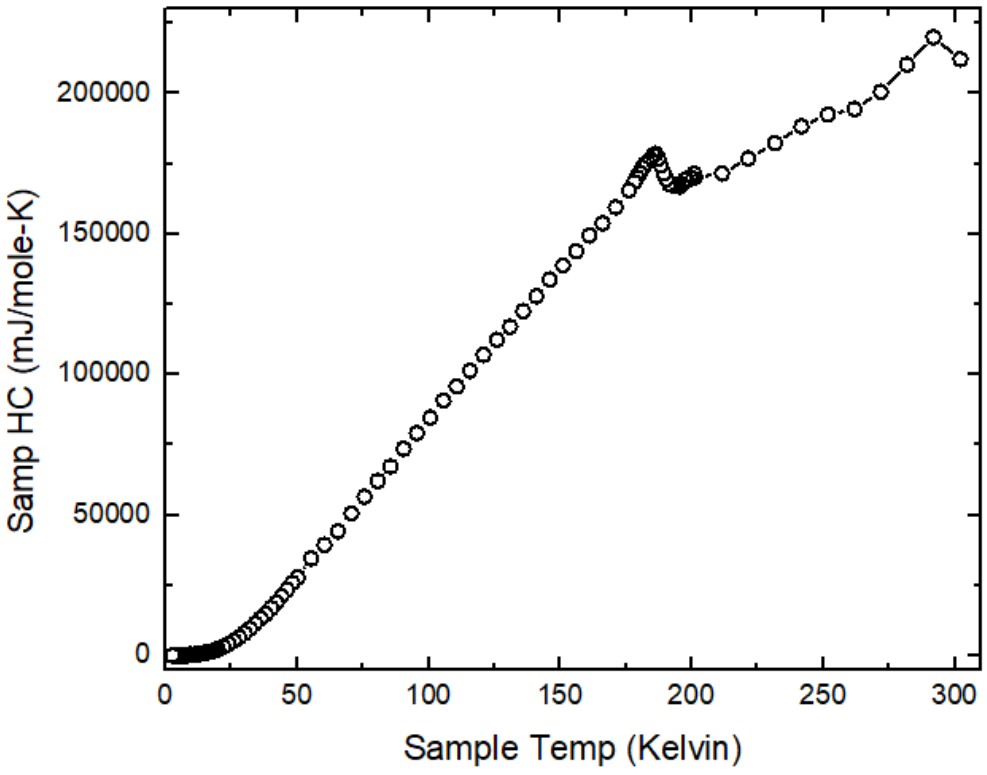

Figure 3.15 Molar heat capacity as a function of temperature shows an anomaly at 186K

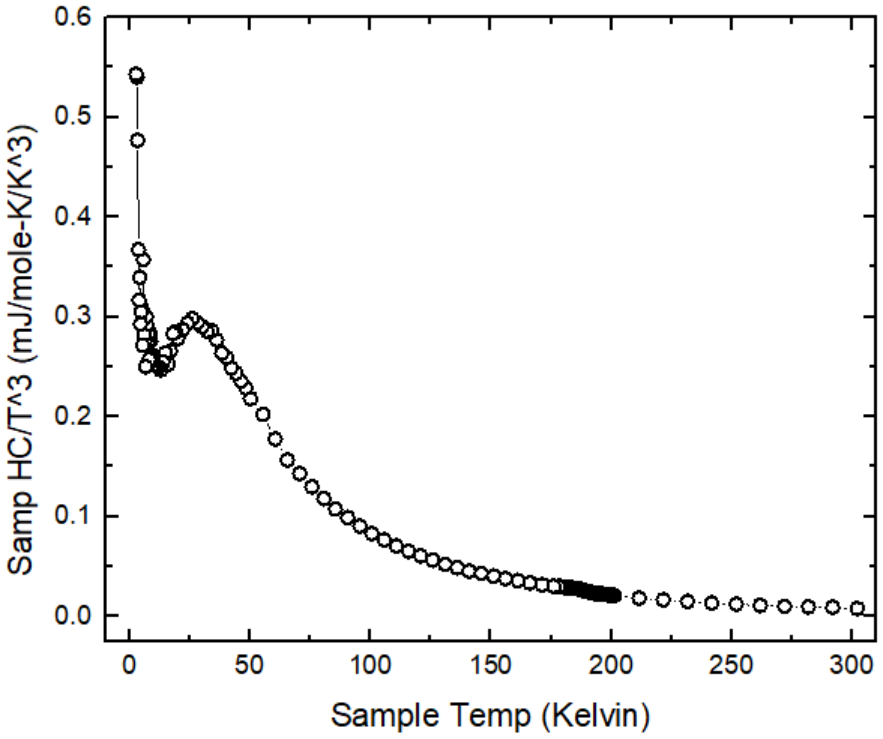

Figure 3.16 C_P/T^3 vs T shows an upturn at low temperature

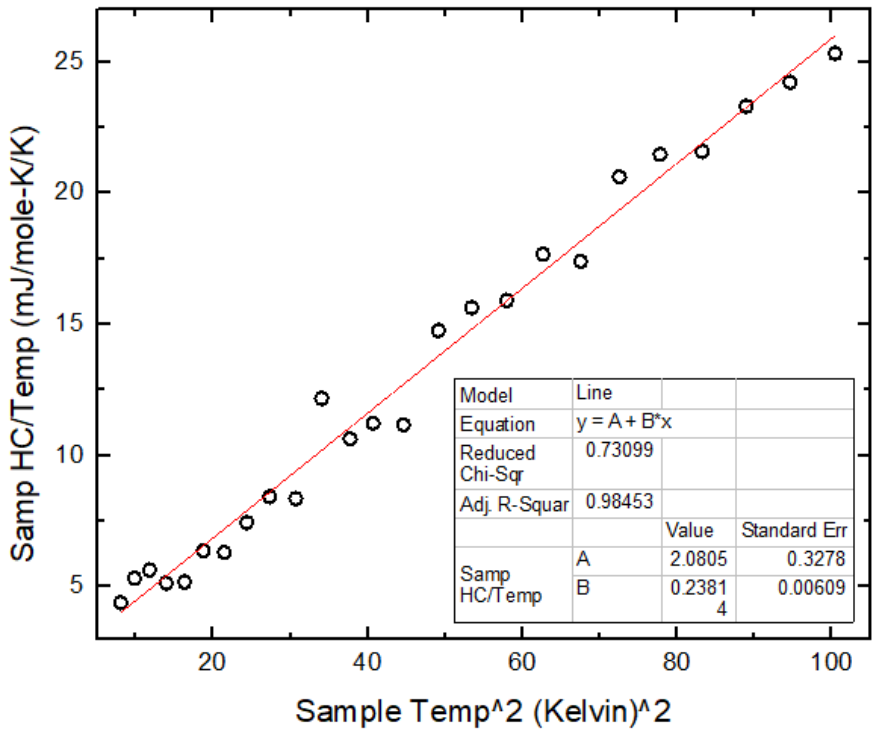

Figure 3.17 Linear fit of C_p/T vs T^2 in the temperature range 3-10K

3.3 Y_2CoIrO_6

3.3.1 Synthesis considerations

Multiple trials have been done for standardizing the synthesis procedure of Y_2CoIrO_6.The temperature sequence and the results of each sintering of Trial1 are shown in Figure 3.18. This reaction was carried out in a box furnace with environment facility (small box furnace) with a ramp rate of 15˚/min. It is concluded that the synthesis temperature of Y_2CoIrO_6 is 1250˚C and at lower temperatures Pyrochlore phase $Y_2Ir_2O_7$ is stable. But similar to Y_2NiIrO_6, staying at 1250˚C for a longer time (even 24 hrs) causes decomposition of sample. Cobalt leaves bright blue color stain on the alumina crucible and on the lid which physically indicates chemical loss. Volatilization of both Iridium and Cobalt oxide leaves excess Y_2O_3 in the system.

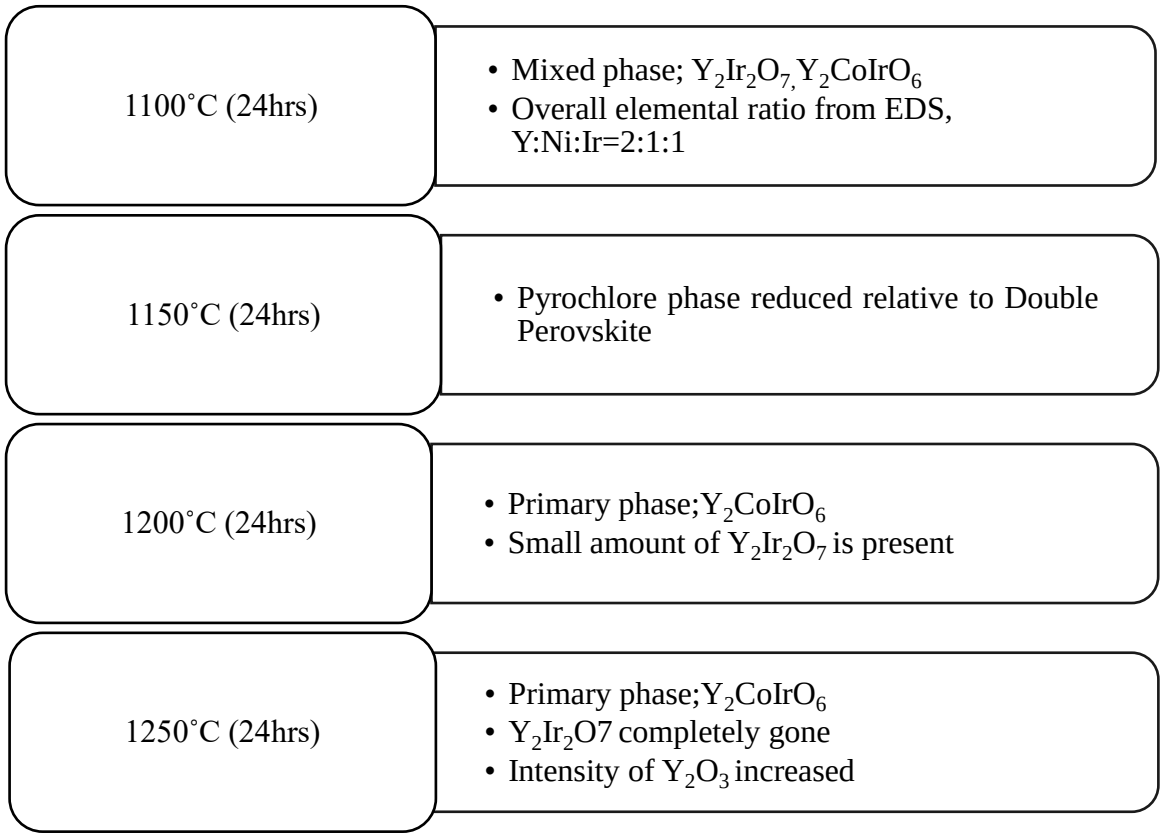

Figure 3.18 Temperature sequence given to Y_2CoIrO_6 trial1 and results of each sintering

Figure 3.19 shows the synthesis procedure for Bulk1. Since a longer time at 1250˚ caused decomposition of the sample, reagent mixture was given short periods of sintering in the small box environment furnace. This gave a mixture of Double Perovskite and Pyrochlore phase in the first two sintering. But later when similar sintering was done in the big box,

peaks of Y_2O_3, Ir metal, IrO_2 emerged. Further sintering led to the oxidation of iridium into iridium oxide. Another trial; Trial2 (not shown here) carried out completely in the big box at 1250˚ for a very short duration gave a decomposed sample, indicating the temperature differences of both furnaces. Bigbox was chosen because of its high ramp rate which will help to eliminate the Pyrochlore phase quickly (as in Y_2NiIrO_6). In Trial3 (Figure 3.20), multiple short treatments were given to the reagent mixture at 1200˚ in the big box furnace with a ramp rate 20˚/min. It yielded Y_2CoIrO_6 as the primary phase along with small peaks of reagents. These reagent peak intensities reduced with sintering but very slowly probably due to insufficient Cobalt oxide in the system.

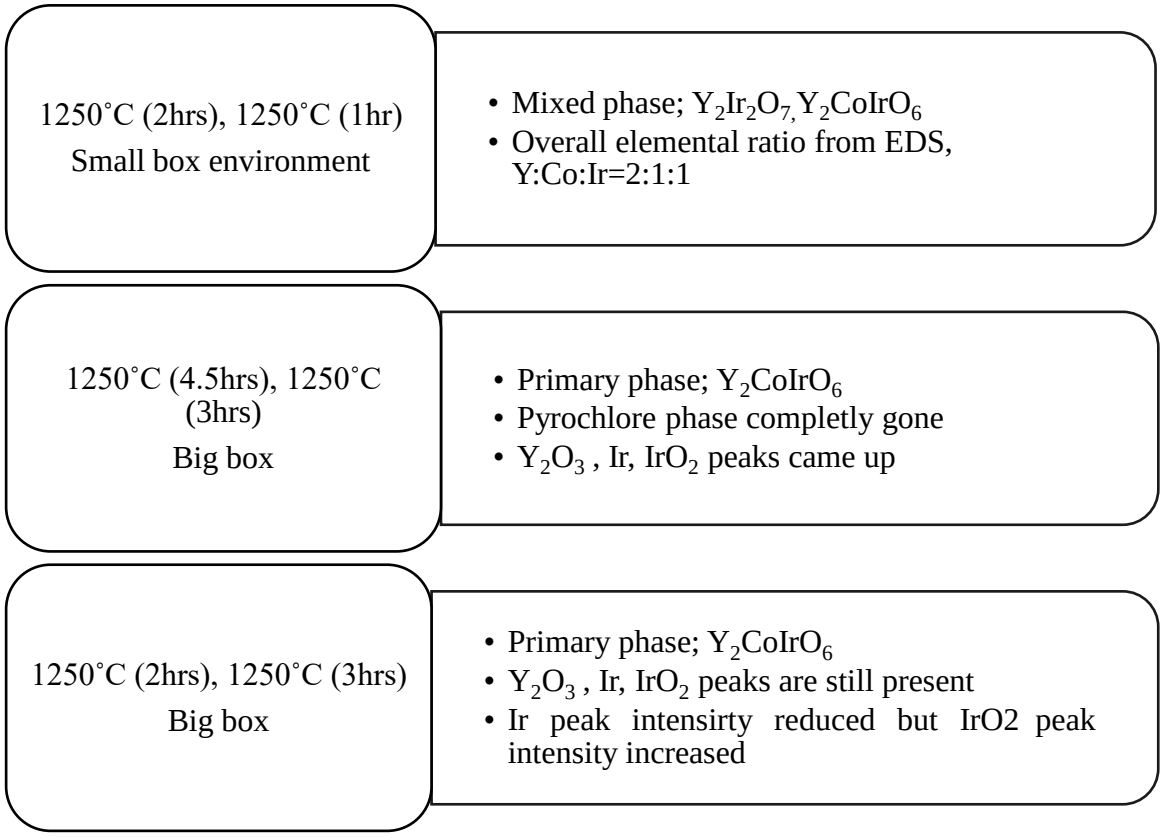

Figure 3.19 Temperature sequence given to Y_2CoIrO_6 Bulk1 and results of each sintering

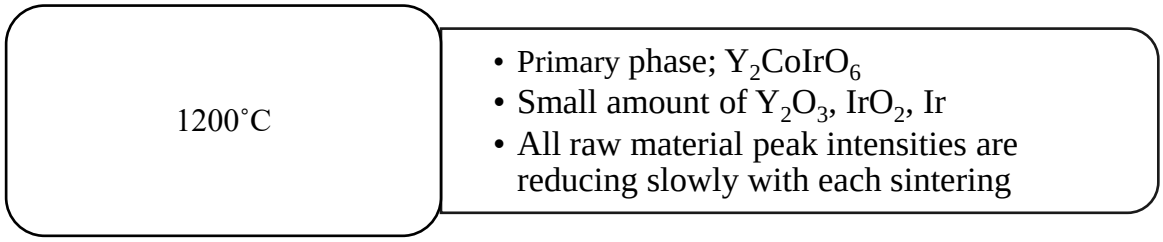

Figure 3.20 Temperature sequence given to Y_2CoIrO_6 Bulk1 and results of each sintering

Following this, the Bulk synthesis of Y_2CoIrO_6 was started (Figure 3.21). First sintering was done in powder form and every other sintering in pellet form. The large surface area in powder form might have resulted in cobalt oxide loss from the system; verified from the bright blue color stains on the crucible and the lid. This along with insufficient oxygen led to an increase in the intensity of Ir peak in the second sintering. Thus the third sintering was done in the tube furnace with O_2 airflow. But the limited ramp rate of tube furnace (6˚C/min) led to the formation of the Pyrochlore phase almost as equal to the Double Perovskite phase. Ir and IrO_2 were used up for the formation of Pyrochlore. Further, one more sintering was given to the sample at 1200˚ in the big box to remove the Pyrochlore phase. Even though Pyrochlore was removed, this increased other raw material peak intensity. Here again Ir content is higher than IrO_2 content due to lack of O_2 in the environment. The room temperature XRD pattern of bulk Y_2CoIrO_6 after second sintering is plotted along with the calculated pattern of Gd_2NiIrO_6 in Figure 3.22.

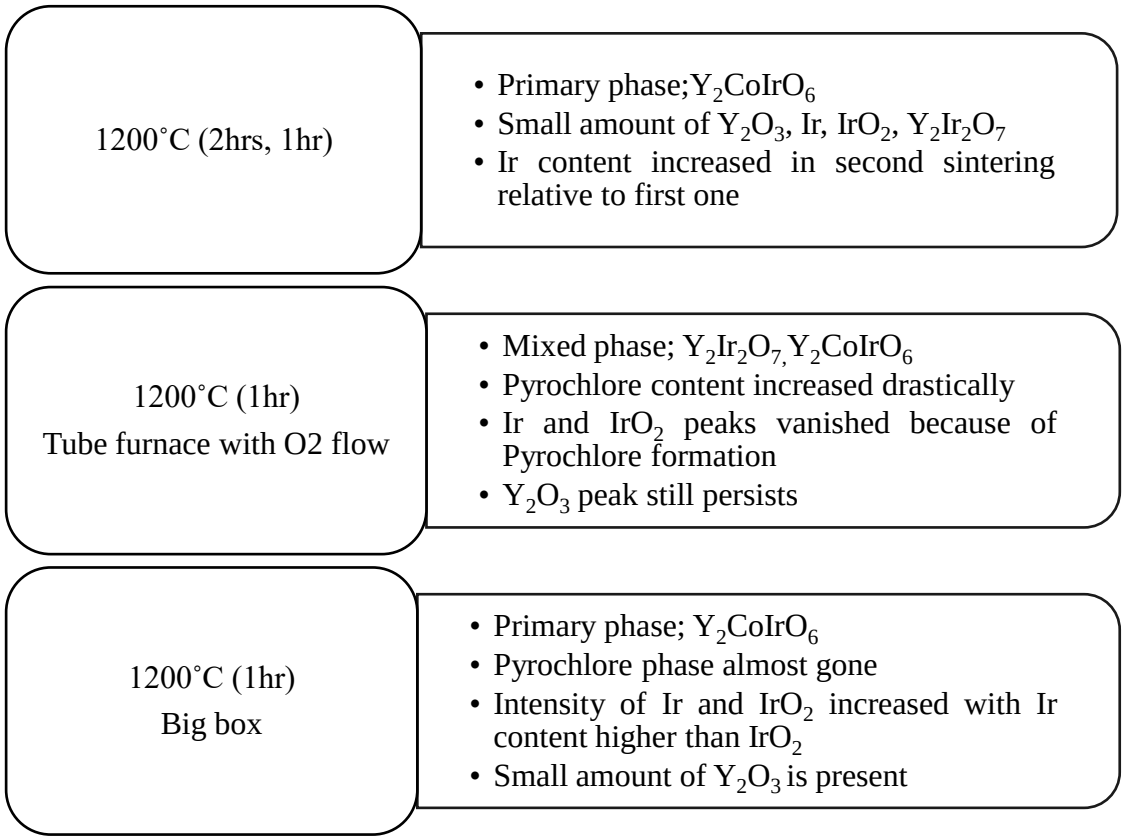

Figure 3.21 Temperature sequence given to Y_2CoIrO_6 bulk and results of each sintering

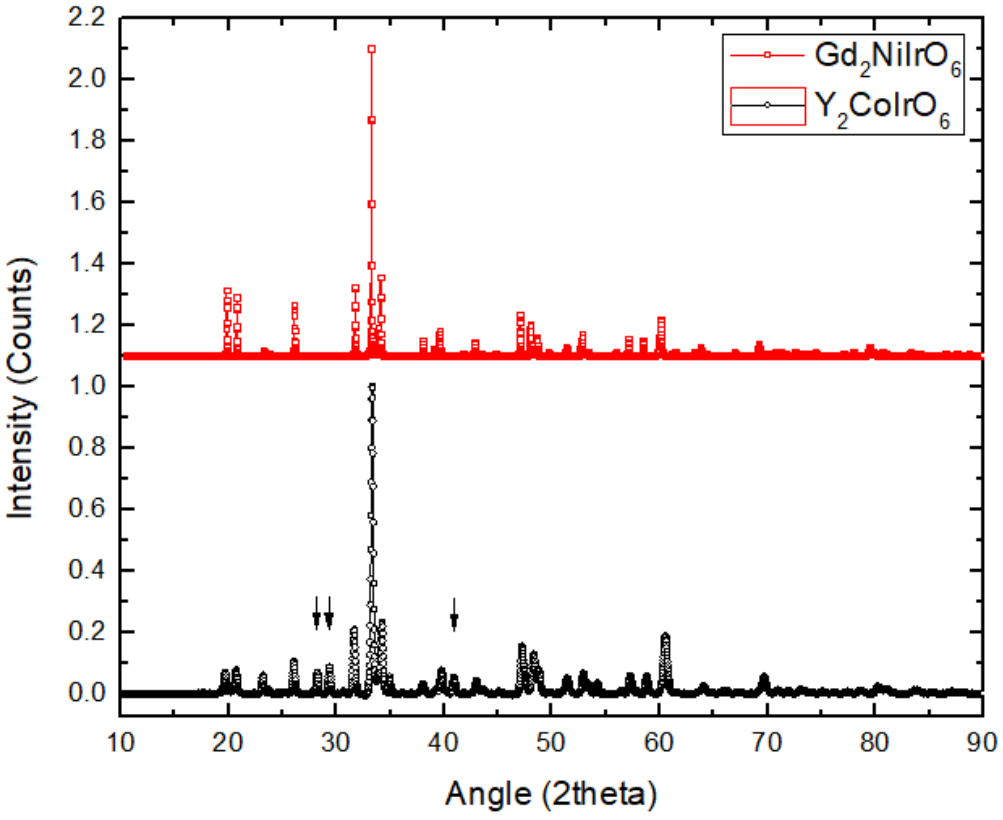

Figure 3.22 A comparison of lab XRD of Y_2CoIrO_6 (black) with reported Gd_2NiIrO_6 (red). Gd_2NiIrO_6 peak positions are X-shifted for comparison. Extra peaks are from raw materials and their primary peaks are marked; Y_2O_3 (222), IrO_2 (110), Ir (111).

Inference from all the trials;

- Synthesis temperature is 1200˚C (in big box)/ 1250˚C (in small box environment)
- At lower temperatures, Pyrochlore phase is stable and at higher temperatures or longer time at the synthesis temperature causes decomposition of the Double Perovskite phase
- To avoid the Pyrochlore phase, a fast ramping is required (20˚C/min)
- The intensity increase of Iridium peak after sintering in the big box furnace could be due to insufficient O_2 in the environment.
- Single-phase formation of Y_2CoIrO_6 is most likely if sintering is done in sufficient airflow with fast ramping
- Sintering needs to be of a short period on pellets of reagent mixture to avoid any chemical loss
- Volatile nature of the reagents (Ir and CoO) might have got enhanced due to phase instability, high temperature, and insufficient O_2 in the environment.

3.4 Conclusions

Two Double Perovskites have been successfully synthesized via solid-state ceramic route. Ba_2FeIrO_6 crystallizes in a hexagonal structure with space group $P6_3/mmc$ (space group no. 194). Due to the similarity in the ionic radii of Ir^{5+} and Fe^{3+}, the compound possess high antisite disorder, nevertheless, the composition of the product is Ba_2FeIrO_6 within the limits of experimental error. A study of molar heat capacity as a function of temperature indicates the presence of a glassy phase. Y_2NiIrO_6 (Tolerance factor, t = 0.8313) crystallizes in monoclinic structure with space group $P2_1/n$. The sharp anomaly at 186K in the molar heat capacity as a function of temperature corroborates the expected high magnetic order temperature. Since its order temperature is between that of Gd_2NiIrO_6 and Lu_2NiIrO_6, we could confirm the magneto-structural coupling observed in this series of compounds [40-41]. Molar heat capacity studies also point into the presence of a glassy phase.

3.5 Future plans

- Structural refinement of Y_2NiIrO_6 has to be done to determine the extent of magneto-structural coupling in the compound
- AC, DC Magnetization measurements are necessary to confirm the nature of transitions and transition temperatures in these compounds
- Other experimental techniques such as dielectric (linear and non-linear) measurement, neutron diffraction, thermal and electronic transport measurements are required for a detailed study of structure-property relationship in these compounds
- Single crystal synthesis of $Y_2(Ni/Co)IrO_6$ is plausible by the flux method as mentioned in [40]. The low sintering temperature and presence of hydroxide flux might lead to a single phase product.

Part 2: Development of an automated susceptometer for non-linear dielectric response measurement (With Shruti Chakravarty)

Chapter 4 Introduction

Dielectric materials are insulators but they become polarized in the presence of an electric field. The polarization (*P*) develops when positive charge carriers in the material align along the direction of the field and the negative carriers align in the opposite direction. Upon removal of the field, material returns to its equilibrium state and time taken for this is called the relaxation time. The dielectric constant ε' represents the extent of electric stress absorbed by the material and that depends on the applied field, frequency of the applied field, temperature, and pressure. An anomaly in the measurement of the dielectric constant as a function of temperature points to the onset of a long-range order (Ferroelectricity) in the system but this could also be due to relaxation of charges or changes in the electrical conductivity. It can also store energy with minimum loss as there are very few free electrons and ferroelectric materials are the best candidate for a capacitor. Since dielectric materials tend to align the dipoles with respect to the applied field/temperature/pressure/frequency they have technological importance as well.

4.1 Non-linear dielectric response

Almost all the studies done so far are focused on the linear dependence of dielectric susceptibility on the applied field; $P = \varepsilon\chi E$, where P is the polarization, E is the applied electric field, ε is dielectric permittivity of the sample, and χ is linear dielectric susceptibility. But in presence of a stronger field or in the vicinity of phase transitions, non-linear terms also come into play [55]:

$$\mathrm{P} = \varepsilon(\chi_1 \mathrm{E}^1 + \chi_2 \mathrm{E}^2 + \chi_3 \mathrm{E}^3 + \cdots) \qquad (4.1)$$

A study of non-linear contribution to the dielectric response could give a lot of physical insights about the system. As said earlier, an anomaly in the temperature dependence of ε' does not confirm the presence of long-range order in the system. Similarly frequency dependence of ε' does not ensure the occurrence of a glassy phase. These can happen also due to the relaxation of charges, changes in electrical conductivity, weakly interacting dipoles, etc. Thus, mere temperature-dependent or frequency-dependent linear ε' is not enough to confirm the ground state of a dielectric system. Here comes the importance of hyper-susceptibility terms. A study by A. Banerjee *et al*. [56-57] concludes linear and non-linear magnetic susceptibility measurements can alone explain the magnetic ground states of the system. Likewise, non-linear terms are helpful in studying dielectric systems as well. In

equation (4.1), the second term is nonzero only in a macroscopically non-centrosymmetric system [58]. Thus χ_2 is proportional to net polarization and it also changes sign when the direction of *P* changes. The magnitude of χ_2 increases as it approaches the Curie temperature T_C and vanishes at T_C. It gives an idea about the strength of polarization and shows up at temperatures above T_C if there is remnant polarization [59]. In spin-glass systems, even terms in the equation (4.1) are absent and hence, χ_2 is useful for a study of mixed phases [60]. Also since χ_2 vanishes at T_C, an accurate determination of Curie temperature is possible. The third order susceptibility exhibits features unique to each type of phase transition [58]. For a continuous ferroelectric (FE) transition, χ_3 changes sign from positive (Ferro phase) to negative (Para phase). Whereas in a discontinuous FE transition or in relaxor FE, χ_3 does not change sign; it is positive throughout the temperature range. But the rapid decrease in magnitude at the T_C distinguishes discontinuous FE from relaxor FE. Thus χ_3 describes the type of ferroelectric transition. From second and third order susceptibilities, another parameter called scaled non-linear susceptibility a_3 is calculated;

$$a_3 = -\frac{1}{{\varepsilon_o}^3}\frac{\chi_3}{{\chi_1}^4}$$

For continuous FE transition, a_3 changes sign from negative (Ferro) to positive (Para) while for discontinuous or relaxor FE transitions, a_3 is negative and does not change the sign. But in discontinuous FE transitions, there is a sudden jump in magnitude at T_C and in relaxor FE the increment is gradual [61]. The thermodynamics of non-linear dielectric response of different systems has been explained in prior literature [59, 62-64].

4.2 Measurement of non-linear susceptibility

Since non-linear susceptibility terms are many orders of magnitude less than that of the linear term, it is difficult to measure them, and hence, are relatively unexplored. In principle, χ vs *E* can be studied in 2 ways:

- By applying a weak probing AC electric field which is superimposed to the variable DC bias field. Changing the DC bias voltage will give differential susceptibility of the sample. Since the AC field is very low and the nonlinearity comes with the DC field, one has restrictions in studying the frequency dependence of non-linear susceptibility.

- By applying a strong AC field to invoke nonlinear terms as well, then a Fourier analysis will help to deduce the different harmonics of the response. But this facility is not commercially available. Also, the applied high field could mask the intrinsic features of the system.

We have tried to implement a method explained by S. Miga *et al*. [65]. The paper proposes measurement of total current (displacive and conductive) passing through the sample when an AC field is applied. A preamplifier (SR570) is used to convert current (I) to voltage (V), which is then fed into a system that can analyze and do a Fast Fourier Transform (FFT) to convert it into the frequency domain. The final output will be the harmonic response of the sample to the applied field and frequency. Figure 4.1 shows the block diagram of the circuit used. Since dielectric materials are in general insulators, contributions from conduction current can be neglected in a qualitative picture.

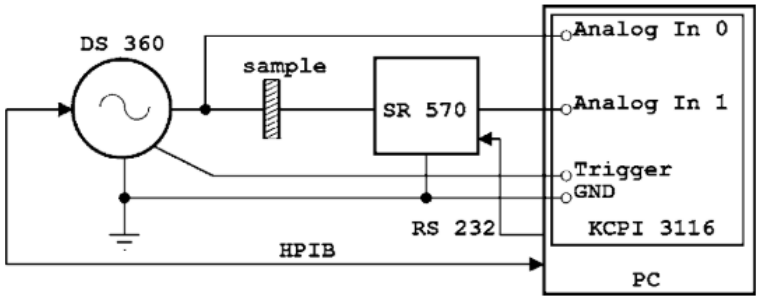

Figure 4.1 Block diagram of the circuit used by S. Miga *et al*. [65]

4.3 Signal analysis

An electric field E of frequency ω is applied to the sample.

$$E(t) = E_0 \sin \omega t$$

Then polarization *P* of the sample becomes,

$$P = \varepsilon_0 \sum_{i=1}^{n} \chi_i E^i(t) = \sum_{i=1}^{n} \chi_i {E_0}^i \sin^i(\omega t)$$

For accurate measurements in a strongly non-linear system, n value up to 7 is considered while calculation. The total current passing through the sample will be

$$I = S \frac{\partial D(t)}{\partial t}$$

Where $D = \varepsilon_0 E + P$, S is the surface area of the electrode

Substitution of polarization equation into the above equation of current will give a set of equations (mentioned in [65]), solving which will provide susceptibility equations;

$$\chi_1 = \frac{1}{\varepsilon_0 S\omega}\left(\frac{d}{U_0}\right)^1 (I_1 + I_3 + I_5 + I_7) - 1$$

$$\chi_2 = \frac{1}{\varepsilon_0 S\omega}\left(\frac{d}{U_0}\right)^2 (I_2 + 2I_4 - 3I_6)$$

$$\chi_3 = \frac{1}{\varepsilon_0 S\omega}\left(\frac{d}{U_0}\right)^3 \left(-\frac{4}{3}I_3 - 4I_5 - 8I_7\right)$$

U_0 = Amplitude of the applied field

d = Thickness of the sample used for measurement

I_i = Harmonic terms of the current measured

More the number of higher-order terms, the better will be the accuracy of the measurement.

4.4 Plan of the thesis

We aim to develop an automated susceptometer for the measurement of linear as well as non-linear dielectric response. The procedure would be modifying the already existing susceptometer for linear dielectric response measurement as per S. Miga *et al* [65] method. Calibration of the measurement set up using standard dielectric samples like KH_2PO_4 (Potassium dihydrogen phosphate) and $BaTiO_3$ has been done.

Chapter 5 Experimental techniques

Figure 5.1 shows the circuit diagram of our non-linear dielectric set-up. An AC voltage is applied on the electrode of the parallel plate capacitor and the current (conductive and displacement current) passing through the sample kept in between the parallel plates is fed into low noise current preamplifier (SR 570). The amplified signal is delivered to the signal analyzer (SR 785). Data analyzed in the SR 785 can be collected through a pen drive or by connecting a computer to the system. To carry out temperature-dependent measurements, a closed cycle refrigerator (CCR), a cryogenic temperature controller and a 50Ω heater have been used. The diffusion pump sets a low vacuum inside the sample chamber. A proper grounding to avoid any ground loop issues, and better solder junctions for assuring good electrical contact were maintained for low noise level measurement.

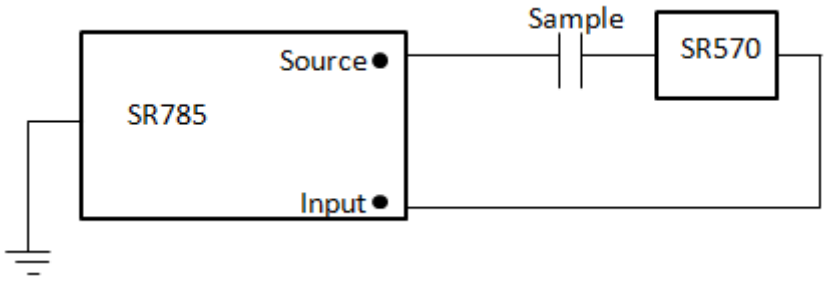

Figure 5.1 Circuit diagram of non-linear dielectric set up

5.1 Circuit components

5.1.1 Closed Cycle Refrigerator (CCR)

In low-temperature systems, generally, a cryo-liquid like liquid N_2 or liquid He is used to lower the temperature. A closed cycle refrigerator does not use cryoliquid instead it has compressed He gas which refrigerates the system by compression and expansion based on Gifford-McMahon (G-M) cycle [66]. CCR includes a cold head, compressor, gas lines, and a sample chamber. G-M cycle happens at the cold head and the compressor delivers high pressure He gas to the cold head. In and out gas lines connect both the compressor and cold head. The compressor needs constant water cooling and hence, is attached to a chiller. The four steps of a G-M cycle are 1) pressurization, where the high-pressure valve of the compressor is open and He gas reaches the cylinder. The regenerator releases the heat as it cools down the warm gas. 2) The displacer moves upward to increase the volume but the pressure remains constant as there is a continuous flow of cold He. 3) Now the high-pressure

valve is closed and the low-pressure valve is open. Some amount of cold He leaves the cylinder, resulting in the expansion of gas. This is where cooling occurs. 4) Displacer moves downward to release remaining gas from the cylinder

5.1.2 Silicon diode sensor and temperature controller

A silicon diode sensor (DT 670 SD) and a Lakeshore 335 temperature Controller have been used to determine the sample temperature. The temperature range of the diode, accuracy, resolution, response time and repeatability are the few things that need to be checked while choosing a sensor. Proper mounting of the sensor, good contact between sensor lead wires and connection wires, and proper thermal anchoring improve the measurement accuracy. Silicon diode sensors have a temperature range of 1.4-500K and they are interchangeable. Sensor and the copper bobbin, around which additional lead wires were wrapped, were fixed using GE Varnish. In diode sensors, the temperature is calculated from the voltage drop across the PN junction as temperature increases at a constant current supply. Lakeshore temperature controller has the standard curve of DT 670 SD installed and from this, any temperature between the range 1.4-500K can be measured.

5.1.3 Sample holder

A spring-loaded parallel plate capacitor configuration (Figure 5.2), compatible with CCR cold head was designed for the linear dielectric response measurement by a former doctoral student [67]. Here the sample is sandwiched between upper and lower electrodes to which the source wire and signal picking wire are connected respectively.

Figure 5.2 Spring-loaded sample holder attached to the cold head of CCR.

To avoid electrical short between electrodes and the CCR cold head, a thin layer of Teflon is attached to the other side of the electrodes. Parallel plate configuration ensures proper thermal contact between the sample and electrodes and dampens the mechanical vibrations due to CCR pumping. This sample holder is attached to the cold head via two copper screws and a thin layer of Apiezon-N grease facilitates good thermal conduction. We had to tune the dimensions of sample holder components to accommodate the temperature lag and the aim was to provide a better thermal path with the least possible thermal mass. The entire conducting path of the sample chamber is made of copper (Cu).

5.1.4 Dynamic Signal Analyzer (SR785)

Any time varying wave can be represented by the weighted sum of pure sine waves of different frequencies. Here, the dynamic signal analyzer computes the frequency spectrum of a time varying wave by the Fast Fourier Transformation (FFT) method. In a non-linear response measurement set up, this instrument is extremely useful in reducing the complications and fastening the process. The Nyquist theorem states that if the sampling rate is higher than twice the highest frequency component of the signal, the output will accurately represent the input time domain wave. The sampling rate of SR785 is 262 kHz; hence frequencies higher than 102.4 kHz are removed before FFT calculation. The sampling rate is the digitization frequency of an input signal in the signal analyzer. The digital time record of the input signal then undergoes FFT and computes the frequency spectrum. As the output is in the frequency domain, noise troubleshooting is also easier.

SR785 has FFT synchronized, ultra-low distortion internal source generator which is used as the source of the sine wave in the non-linear measurement set up. A source with ultra-low distortion is preferred since the nonlinearity is expressed in harmonics of the applied field. The maximum frequency and amplitude of the source is 102.4 kHz and 5 Vpk respectively. Generally, for measurement, non-multiplier of the line frequency is chosen to avoid line voltage contribution.

5.1.5 Low-Noise Current Preamplifier (SR570)

SR570 converts the input current into a proportional voltage. The amplification does not degrade the signal to noise ratio. Its maximum current input is $\pm$ 5 mA and the sensitivity options range from 1pA/V- 1mA/V to control signal amplification. For best performance, input current should produce a voltage less than or equal to 1V and an output voltage greater than 7V overloads the instrument. Also, offset current, frequency filters, inversion, gain mode

options are available. For sensitive measurements, the instrument can be used in battery mode. A low noise current preamplifier is preferred over a resistive termination of the current source and then amplifying the voltage by voltage preamplifier as the former provides better amplitude and phase accuracy. For our measurements; 20μA/V or 50μA/V sensitivity and low noise gain mode were used.

5.1.6 Diffusion Pump

The diffusion pump is used to create a vacuum of the order 10^{-6} mbar inside the sample chamber. It works on the principle of gas diffusion. The silicone oil inside the pump is boiled and the vapors are compressed as it moves upward inside a vertically tapering hollow cone. This releases high speed oil droplets through the multi-stage jet assembly. Oil droplets impart momentum on the air molecules and drive them towards the bottom of the chamber. This creates a pressure difference inside the pump and air molecules at the bottom of the chamber are sucked by the rotary pump. Filling liquid N_2 in the dewar surrounding this high vacuum chamber accelerates the process by allowing fast condensation of oil droplets. An additional advantage of the diffusion pump is that it is vibration-free.

5.2 Measurement protocol

A thin pellet (thickness~0.8mm, diameter~13mm) of a known sample with Ag coating is loaded and measurements are taken for various applied voltages and frequencies. At any particular temperature T, measurements are taken for V1F1, and V1F2, V2F1, V2F2. The temperature range for these measurements is 20K to 300K. Effect of pellet thickness, quality of vacuum and silver coating was observed during the calibration process. The measurement was automated at a later stage. The program was written using LabView with the help of Mr. Anil Prathamashetti (Technical Staff, Physics Department).

5.3 Calibration

Standard samples; KH_2PO_4 (Potassium dihydrogen phosphate) and $BaTiO_3$ were used for the calibration of the instrument. Polycrystalline KH_2PO_4 (KDP) from Sigma Aldrich was ground and pelletized. KDP is a standard FE material. It undergoes para to ferroelectric transition at 123 K and shows a glassy feature around 75 K [68]. We did the measurement on KDP thin pellet (t~ 0.8mm) with Ag coating. $BaTiO_3$ was synthesized in the lab via solid-state method in pellet form. It is a standard Ferroelectric (FE) material which shows para- to ferroelectric transition at around 200K [69].

Chapter 6 Results and discussions

6.1 Calibration

Calibration measurements have been done on KDP and BTO pellets of thickness around 8-9mm. Since the mere KDP pellet gave a very weak signal, silver paste was coated on both sides of the pellet for all measurements. Also, all electrical wirings have been redone to reduce the noise contribution to the signal. A measurement on KDP pellet (Figure 6.1) showed the transition at 64K indicating a temperature lag of around 60K. Figure 6.2 shows the variation of the signal magnitude with the temperature at a source voltage of 3V and different frequencies. Thus the anomaly at 64K doesn't have frequency dependence.

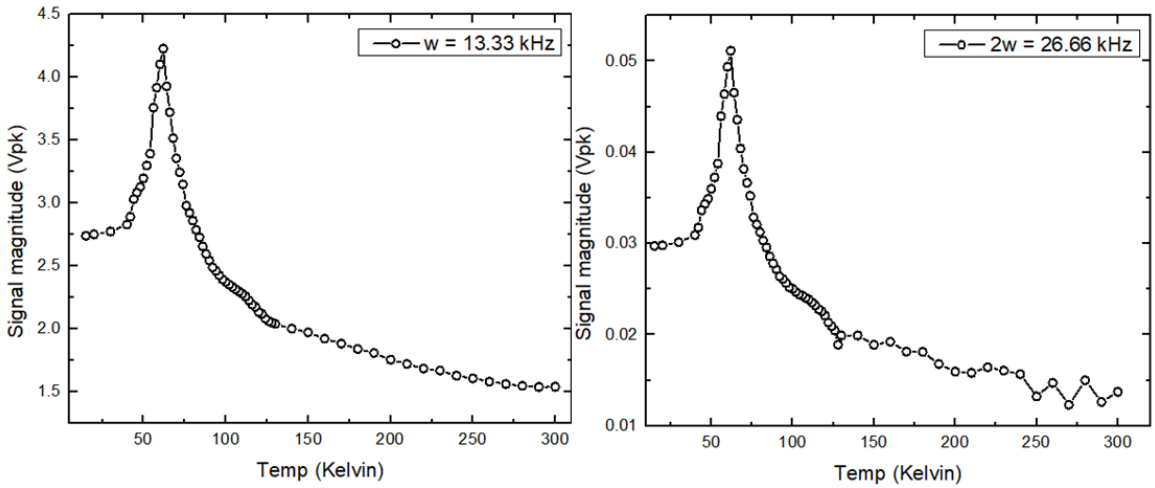

Figure 6.1 Temperature dependence of Signal Magnitude at ω (left) and 2ω (right), ω= 13.33 KHz, Voltage= 1V

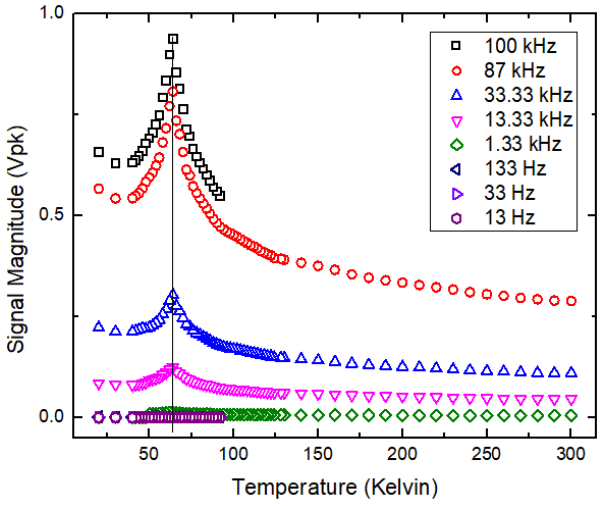

Figure 6.2 Temperature dependence of Signal Magnitude at V=3V and different frequencies (Normalized)

Polishing the copper components of the sample chamber to remove the oxide layer has increased the transition temperature to 81K. We conducted the measurement in a low vacuum (~10^{-3} mbar) but did not improve the thermal lag. In further efforts to improve the thermal path, we used Mylar tape, a thermally conducting electrically insulating tape, to connect upper and lower parts of the sample chamber. This improved the thermal conductivity and the peak appeared at 118K. A subtle glassy feature is visible at around 75K. We also obtained a noisy second harmonic signal. Figure 6.3 shows the data obtained using Mylar tape.

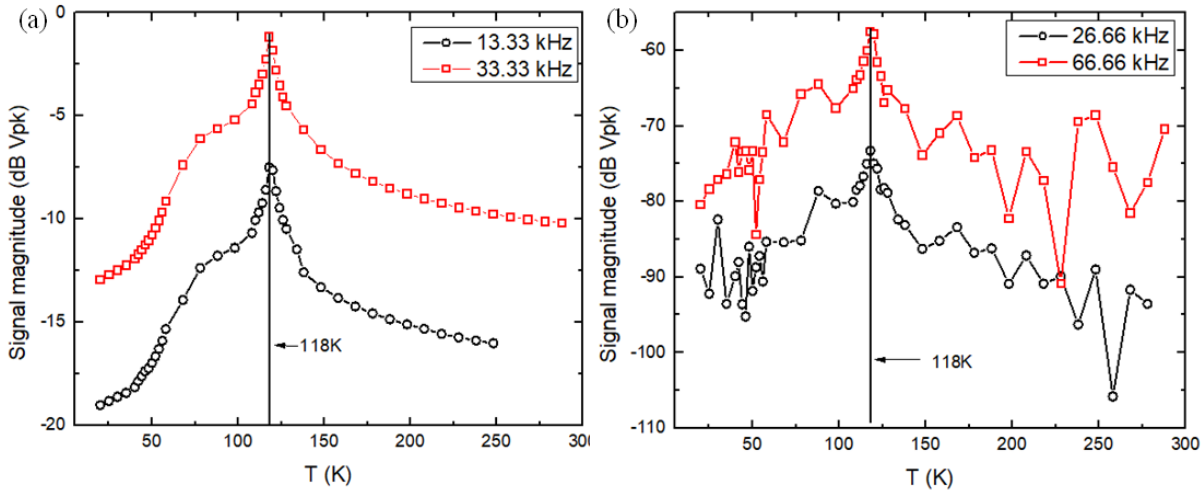

Figure 6.3 First harmonic response of KDP at Voltage V=1V (left) second harmonic response of KDP at Voltage V=1V (right)

A major problem we faced during the calibration of the instrument was the incompatibility of locally procured stainless steel springs towards thermal cycles. The purpose of the spring in this set up is to push the lower electrode upward against the compressions of CCR. But at lower temperatures, the spring becomes soft and is unable to push the lower electrode. Hence the lower electrode and the sample lose contact with the upper electrode. This creates fluctuations in the measured signal or sudden drop in the signal magnitude. Hard springs (stainless steel) seemed to do better, but continuous thermal cycles worsen their performance as well. To solve this, we used a hard spring and gave it few thermal shocks by putting it in liquid N_2. Since, it maintained the hardness even after this, further measurements were carried out using this spring. The dimensions of the sample holder components were changed to improve the thermal contact. A better contact of KDP pellet with the electrodes itself improved the thermal path and the peak appeared at 114K (Figure 6.4 (a)). Application of N-apiezon grease at the thermal junctions, and covering thermal gaps using mylar tapes shifted the peak to 116K (Figure 6.4 (b)).

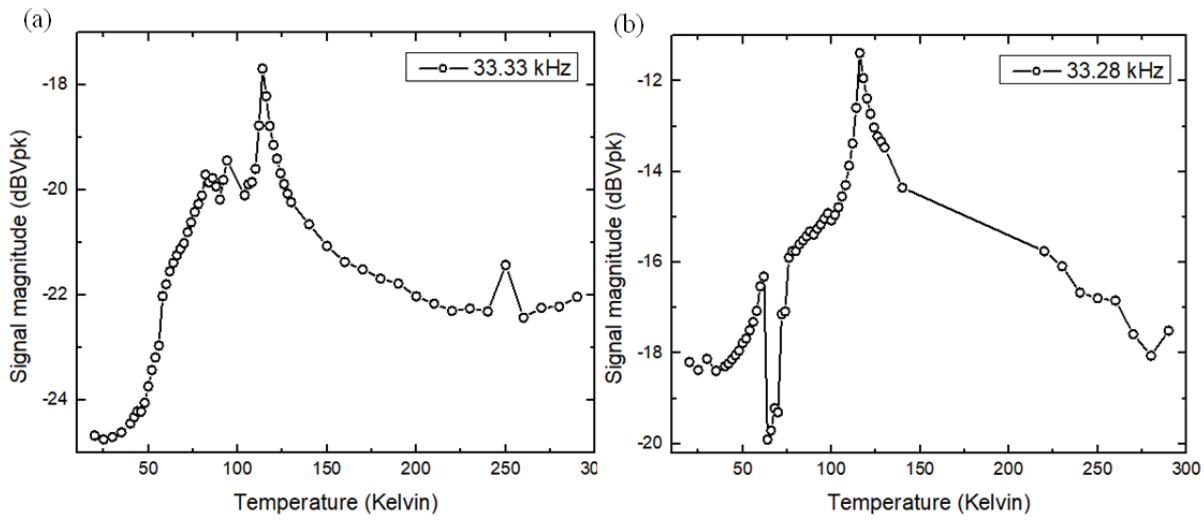

Figure 6.4 Signal magnitude as a function of temperature measured using a stiff stainless steel spring (a) First measurement with the spring (b) the second measurement done using the same spring

Part of the mechanical disturbance still remained is the signal fluctuation in the range 70-100K. In the earlier measurements, signal magnitude exhibited a random hike or drop in this temperature regime. Since, a similar trend is present in BTO measurement (Figure 6.5) as well, this is most likely due to the mechanical disturbance.

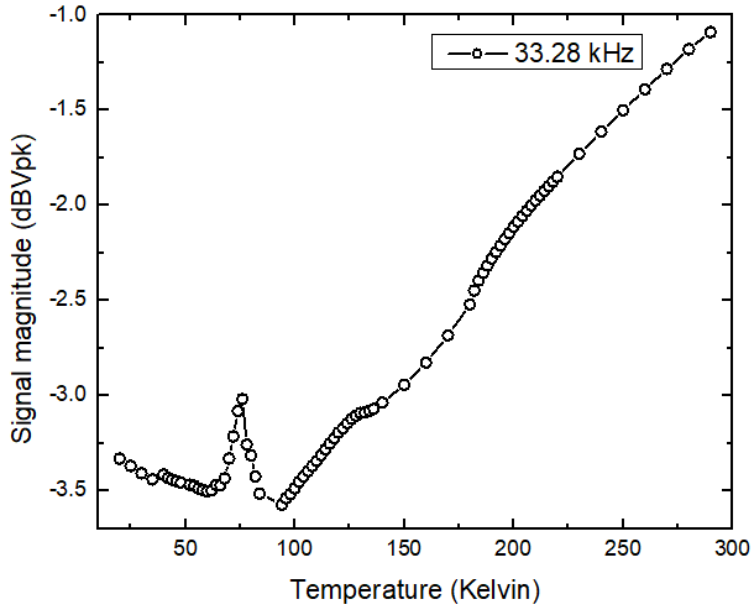

Figure 6.5 Measurement on BTO pellet at a source voltage of 0.5Vpk and 33.33 kHz

Also, these fluctuations increase as the spring undergoes several thermal cycles. This is evident from Figure 6.4 (a) and (b). With the same spring, signal magnitude suddenly drops

at around 70K in the second measurement, shown in Figure 6.4 (b). The main purpose of upper and lower copper plates (electrodes) is to provide a thermal path for doing the temperature-dependent measurement. Avoiding these copper plates in the electronic path might resolve this issue. That is to connect the source and signal picking wires directly to the pellet.

6.2 Manual vs Programmed data acquisition

Figure 6.6 depicts a comparison between manual and automatic data acquisition of a 0.9 mm thick Ag-coated KDP pellet. A peak appears at 81K (closer to the expected value of 123K) in the first harmonic signal possibly because the electrodes have been polished well to remove oxide layers resulting in improved thermal conduction. The mismatch between the magnitude of the signal below 100K is due to the change in the gain of SR570 in order to avoid overloading the amplifier. But above 100K, the measured signal values overlap, indicating robustness in the programmed data acquisition.

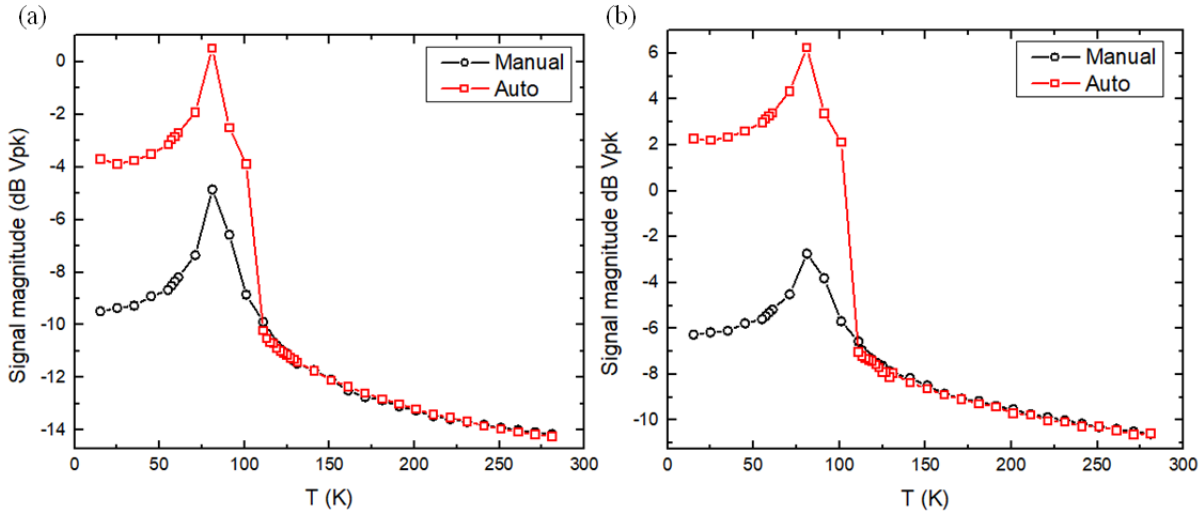

Figure 6.6 (a) First harmonic response of KDP for Voltage V=1V, ω= 13.33 kHz (b) First harmonic response of KDP for Voltage V= 1V, ω= 33.33 kHz

Advantages of this measurement method are listed below;

1. Simultaneous measurement of linear and non-linear susceptibilities
2. It enables measurement in low AC (Alternating current) field that too without any DC field requirement (Direct Current)
3. With the I to V converter, any capacitive voltage dividers are not required in the circuit and hence, unwanted phase shifts are avoided.

4. Measurement can be carried out in a temperature range of 15-300K
5. SR785 source can generate AC signals with a maximum frequency of 102.4 kHz, with amplitude up to 5V.
6. The entire measurement procedure is automated using the Lab-View program.

6.3 Conclusion

During the calibration of the setup, we could reduce the thermal lag from an initial value of 60K to 7K. In the latest measurement of the first harmonic response of KDP, the transition peak appeared at 116K. We could also finish the automation of the susceptometer successfully.

6.4 Future plans

1. Improving the thermal path between the upper and lower parts of the sample chamber by adding one more copper screw while taking care of the thermal mass.
2. Remove the parallel copper plates from the electrical pathway to avoid any mechanical disturbance in the signal measurement.
3. Calibration of the non-linear dielectric susceptibility measurement setup using other standard FE samples/relaxor ferroelectrics.
4. After proper calibration, noise sources need to be removed for better measurement of higher harmonic signals.
5. Measurement of the linear and non-linear dielectric susceptibility of Y_2NiIrO_6 and Ba_2FeIrO_6 specimens synthesized during the course of this thesis.

References

1. D. Giovanni, Optical-Spin Dynamics in Organic-Inorganic Hybrid Lead Halide Perovskites, Nanyang Technological University, 2017.
2. E. Olsson, X. Aparicio-Anglès, and N.H. De Leeuw, J. Chem. Phys. **145**, 014703 (2016).
3. S. Vasala and M. Karppinen, Prog. Solid State Chem. **43**, 1 (2015).
4. E. Reynolds, B.J. Kennedy, G.J. Thorogood, D.J. Gregg, and J.A. Kimpton, J. Nucl. Mater. **433**, 37 (2013).
5. M.W. Lufaso and P.M. Woodward, Acta Crystallogr. Sect. B Struct. Sci. **60**, 10 (2004).
6. V.M. Goldschmidt, Naturwissenschaften **14**, 477 (1926).
7. P. Kayser, J.A. Alonso, A. Muñoz, and M.T. Fernández-Díaz, Acta Mater. **126**, 114 (2017).
8. M. Retuerto, J.A. Alonso, M.J. Martínez-Lope, M. García-Hernández, K. Krezhov, I. Spirov, T. Ruskov, and M.T. Fernández-Díaz, Eur. J. Inorg. Chem. **2008**, 2286 (2008).
9. Z. Fang, K. Terakura, and J. Kanamori, Phys. Rev. B **63**, 180407 (2001).
10. P. Karen, A.R. Moodenbaugh, J. Goldberger, P.N. Santhosh, and P.M. Woodward, J. Solid State Chem. **179**, 2120 (2006).
11. D.D. Sarma, E. V. Sampathkumaran, S. Ray, R. Nagarajan, S. Majumdar, A. Kumar, G. Nalini, and T.N. Guru Row, Solid State Commun. **114**, 465 (2000).
12. R.P. Singh and C. V. Tomy, Phys. Rev. B **78**, 024432 (2008).
13. P.K. Davies, H. Wu, A.Y. Borisevich, I.E. Molodetsky, and L. Farber, Annu. Rev. Mater. Res. **38**, 369 (2008).
14. P.D. Battle, J.B. Goodenough, and R. Price, J. Solid State Chem. **46**, 234 (1983).
15. M. Retuerto, M. García-Hernández, M.J. Martínez-Lope, M.T. Fernández-Díaz, J.P. Attfield, and J.A. Alonso, J. Mater. Chem. **17**, 3555 (2007).
16. R. Wiebe, E. Greedan, P. Kyriakou, M. Luke, S. Gardner, A. Fukaya, M. Gat-Malureanu, L. Russo, T. Savici, and J. Uemura, Phys. Rev. B **68**, 134410 (2003).
17. J.G. Cheng, G. Li, L. Balicas, J.S. Zhou, J.B. Goodenough, C. Xu, and H.D. Zhou, Phys. Rev. Lett. **107**, 197204 (2011).
18. R. Morrow, R. Mishra, O.D. Restrepo, M.R. Ball, W. Windl, S. Wurmehl, U. Stockert, B. Büchner, and P.M. Woodward, J. Am. Chem. Soc. **135**, 18824 (2013).

19. C. Ritter, M.R. Ibarra, L. Morellon, J. Blasco, J. García, and J.M. De Teresa, J. Phys. Condens. Matter **12**, 8295 (2000).
20. G. Cao, J.E. Crow, R.P. Guertin, P.F. Henning, C.C. Homes, M. Strongin, D.N. Basov, and E. Lochner, Solid State Commun. **113**, 657 (2000).
21. G. Cao, Y. Xin, C.S. Alexander, J.E. Crow, P. Schlottmann, M.K. Crawford, R.L. Harlow, and W. Marshall, Phys. Rev. B **66**, 1 (2002).
22. G. Cao, J. Bolivar, S. McCall, J. Crow, and R. Guertin, Phys. Rev. B **57**, R11039 (1998).
23. G. Cao and P. Schlottmann, Reports Prog. Phys. **81**, 042502 (2018).
24. S.J. Moon, H. Jin, K.W. Kim, W.S. Choi, Y.S. Lee, J. Yu, G. Cao, A. Sumi, H. Funakubo, C. Bernhard, and T.W. Noh, Phys. Rev. Lett. **101**, 226402 (2008).
25. X. Liu, V.M. Katukuri, L. Hozoi, W.G. Yin, M.P.M. Dean, M.H. Upton, J. Kim, D. Casa, A. Said, T. Gog, T.F. Qi, G. Cao, A.M. Tsvelik, J. Van Den Brink, and J.P. Hill, Phys. Rev. Lett. **109**, (2012).
26. S. Bhowal, S. Baidya, I. Dasgupta, and T. Saha-Dasgupta, Phys. Rev. B **92**, 121113 (2015).
27. O.N. Meetei, W.S. Cole, M. Randeria, and N. Trivedi, Phys. Rev. B **91**, 054412 (2015).
28. G. Cao, T.F. Qi, L. Li, J. Terzic, S.J. Yuan, L.E. Delong, G. Murthy, and R.K. Kaul, Phys. Rev. Lett. **112**, 056402 (2014).
29. J. Terzic, H. Zheng, F. Ye, H.D. Zhao, P. Schlottmann, L.E. De Long, S.J. Yuan, and G. Cao, Phys. Rev. B **96**, 064436 (2017).
30. E. Vincent and V. Dupuis, in *Frustrated Materials and Ferroic Glasses*, edited by T. Lookman and X. Ren (Springer International Publishing, Cham, 2018), pp. 31–56.
31. J.A. Mydosh, Reports Prog. Phys. **78**, 052501 (2015).
32. C.A.M. Mulder, A.J. Van Duyneveldt, and J.A. Mydosh, Phys. Rev. B **23**, 1384 (1981).
33. S. Nagata, P.H. Keesom, and H.R. Harrison, Phys. Rev. B **19**, 1633 (1979).
34. G.E. Brodale, R.A. Fisher, W.E. Fogle, N.E. Phillips, and J. van Curen, J. Magn. Magn. Mater. **31**–**34**, 1331 (1983).
35. J.B. MacChesney, J.F. Potter, R.C. Sherwood, and H.J. Williams, J. Chem. Phys. **43**, 3317 (1965).
36. A. V. Powell and P.D. Battle, J. Alloys Compd. **191**, 313 (1993).

37. N.A. Jordan, P.D. Battle, J. Sloan, P. Manuel, and S. Kilcoyne, J. Mater. Chem. **13**, 2617 (2003).
38. P.D. Battle, G.R. Blake, T.C. Gibb, and J.F. Vente, J. Solid State Chem. **145**, 541 (1999).
39. T. Ferreira, D. Carone, A. Huon, A. Herklotz, S.A. Stoian, S.M. Heald, G. Morrison, M.D. Smith, and H.C. Zur Loye, Inorg. Chem. **57**, 7362 (2018).
40. T. Ferreira, G. Morrison, J. Yeon, and H.-C. Zur Loye, Cryst. Growth Des **16**, 2795 (2016).
41. H.L. Feng, Z. Deng, M. Wu, M. Croft, S.H. Lapidus, S. Liu, T.A. Tyson, B.D. Ravel, N.F. Quackenbush, C.E. Frank, C. Jin, M.R. Li, D. Walker, and M. Greenblatt, Inorg. Chem. **58**, 397 (2019).
42. P.M. Woodward, Acta Crystallogr. Sect. B Struct. Sci. **53**, 32 (1997).
43. R.A. Young, *The Rietveld Method* (Oxford University Press, 1995).
44. Q. Design, *Physical Property Measurement System, Heat Capacity Option User's Manual* (1999).
45. A. Banerjee, R. Rawat, K. Mukherjee, and P. Chaddah, Phys. Rev. B **79**, 212403 (2009).
46. S.J. Mugavero, A.H. Fox, M.D. Smith, and H.C. zur Loye, J. Solid State Chem. **183**, 465 (2010).
47. S.J. Mugavero, M.D. Smith, and H.C. Zur Loye, J. Solid State Chem. **178**, 200 (2005).
48. M.J. Davis, S.J. Mugavero, K.I. Glab, M.D. Smith, and H.C. Zur Loye, Solid State Sci. **6**, 413 (2004).
49. A. Hossain, P. Bandyopadhyay, and S. Roy, J. Alloys Compd. **740**, 414 (2018).
50. P.A. Seinen, F.P.F. van Berkel, W.A. Groen, and D.J.W. Ijdo, Mater. Res. Bull. **22**, 535 (1987).
51. K. Ouchetto, F. Archaimbault, J. Choisnet, and M. Et-Tabirou, Mater. Chem. Phys. **51**, 117 (1997).
52. X. Ding, B. Gao, E. Krenkel, C. Dawson, J.C. Eckert, S.W. Cheong, and V. Zapf, Phys. Rev. B **99**, 1 (2019).
53. P. Kayser, J.A. Alonso, A. Muñoz, and M.T. Fernández-Díaz, Acta Mater. **126**, 114 (2017).
54. P.M. Woodward, Acta Crystallogr. Sect. B Struct. Sci. **53**, 32 (1997).

55. S. Miga, J. Dec, W. Kleemann, in *Ferroelectrics: Characterization and Modeling*, edited by L. Mickaël (InTech, 2011), pp. 181–203.
56. A. Banerjee, A. Bajpai, and S. Nair, in *Frontiers in Magnetic Materials*, edited by A.V. Narlikar (Springer, Berlin, Heidelberg, 2005), pp. 43–69.
57. S. Nair and A. Banerjee, Phys. Rev. B **68**, 094408 (2003).
58. S. Miga and J. Dec, Ferroelectrics **367**, 223 (2008).
59. S. Ikeda, H. Kominami, K. Koyama, and Y. Wada, J. Appl. Phys. **62**, 3339 (1987).
60. A. Chakravarti, R. Ranganathan, and C. Bansal, Solid State Commun. **82**, 591 (1992).
61. J. Dec, W. Kleemann, V. Bobnar, Z. Kutnjak, A. Levstik, R. Pirc, and R. Pankrath, Europhys. Lett. **55**, 781 (2001).
62. S. Ikeda, H. Suzuki, K. Koyama, and Y. Wada, Polym. J. **19**, 681 (1987).
63. X. Wei and X. Yao, Int. J. Mod. Phys. B **20**, 2977 (2006).
64. I.P. Kaminow, Proc. IEEE **66**, 1299 (2008).
65. S. Miga, J. Dec, and W. Kleemann, Rev. Sci. Instrum. **78**, 033902 (2007).
66. W.E. Gifford, Adv. Cryog. Eng. **11**, 152 (1966).
67. S.N. Panja, Magnetic and Polar Properties of Some Geometrically Frustrated Transition Metal Oxides, IISER PUNE, 2018.
68. H. Motegi, K. Kuramoto, E. Nakamura, K. Hayashi, and I. Kitayama, J. Phys. Soc. Japan **54**, 2735 (1985).
69. A. Von Hippel, Rev. Mod. Phys. **22**, 221 (1950).